Editors' Suggestion

Field-temperature phase diagram of the enigmatic $Nd_2(Zr_{1-x}Ti_x)_2O_7$ pyrochlore magnets

M. Léger,[1,2,*] E. Lhotel,[1,†] E. Ressouche,[3] K. Beauvois,[3,4] F. Damay,[2] C. Paulsen,[1] A. Al-Mawla,[1] E. Suard,[4] M. Ciomaga Hatnean,[5] G. Balakrishnan,[5] and S. Petit[2,‡]

[1]*Institut Néel, CNRS and Université Grenoble Alpes, 38000 Grenoble, France*

[2]*Laboratoire Léon Brillouin, Université Paris-Saclay, CNRS, CEA, CE-Saclay, F-91191 Gif-sur-Yvette, France*

[3]*IRIG, CEA and Université Grenoble Alpes, CEA Grenoble, F-38054 Grenoble, France*

[4]*Institut Laue Langevin, F-38042 Grenoble, France*

[5]*Department of Physics, University of Warwick, Coventry CV4 7AL, United Kingdom*

(Received 29 April 2021; revised 7 June 2021; accepted 8 June 2021; published 28 June 2021)

By combining neutron scattering and magnetization measurements down to 80 mK, we determine the (H, T) phase diagram of the $Nd_2(Zr_{1-x}Ti_x)_2O_7$ pyrochlore magnet compounds. In those samples, Zr is partially substituted by Ti, hence tuning the exchange parameters and testing the robustness of the various phases. In all samples, the ground state remains all in/all out, while the field induces phase transitions toward new states characterized by two in–two out or one out–three in/one in–three out configurations. These transitions manifest as metamagnetic singularities in the magnetization versus field measurements. Strikingly, it is found that moderate substitution reinforces the stability of the all in/all out phase: the Néel temperature, the metamagnetic fields along with the ordered magnetic moment, are higher in substituted samples with $x < 10\%$.

DOI: 10.1103/PhysRevB.103.214449

I. INTRODUCTION

The last decades of research in the field of condensed matter have seen the emergence of a rich and new physics, going beyond the Néel paradigm and transcending conventional descriptions based on Landau's theory. Frustrated magnetism has largely contributed to these developments, pointing to the existence of new states of matter, such as spin liquids or Coulomb phases. The interest in these states originates from the fact that they host fractional excitations, are described by emergent gauge fields, and exhibit large-scale quantum entanglement [1–3].

The pyrochlore network, built from tetrahedra joined by their vertices, has played a key role in this field. In particular, Ising spins located at the summits of these tetrahedra and coupled by ferromagnetic interactions form an unconventional state called spin ice [4]. The spins remain disordered but nevertheless obey a local rule known as the two in-two out rule, which stipulates that each tetrahedron must have two incoming and two outgoing spins, in close analogy with the disorder of hydrogen atoms in water ice. It results in a residual entropy at zero temperature [5], as well as in a peculiar local organization of the spins. The latter can be observed by neutron scattering and manifests as an elastic pattern in reciprocal space with bow-tie singularities also called pinch points [6–8]. Furthermore, the ice rule can be interpreted as the zero divergence condition of an emergent magnetic field ($\nabla \cdot \mathbf{B} = 0$), a mapping that has allowed considerable theoretical development.

In most of the pyrochlore materials of interest today, the spin is due to the $4f$ magnetic moment of a rare earth. These compounds have been abundantly investigated in the literature [3], with the description of a large variety of ground states arising from the interplay between magnetic exchange couplings, dipolar interactions, and single-ion anisotropy of the magnetic moment. It is worth mentioning spin ices but also spin liquids, fragmented states, and apparently more conventional magnets.

Among them, $Nd_2Zr_2O_7$ has attracted much attention. As inferred from a positive Curie-Weiss temperature, indicating ferromagnetic interactions, and combined with an Ising anisotropy, a spin ice ground state is expected in this material [9,10]. Indeed, the expected pinch point pattern is observed below 1 K [11]. Upon further cooling, however, the spin ice state gives way to an all in/all out (AIAO) ground state, with all the spins pointing out or into each tetrahedron, hence highlighting dominant antiferromagnetic interactions [9,10,12].

Motivated by this very rich physics and by the competition between spin ice and the AIAO state [13,14], we investigate in this paper the field-temperature (H, T) phase diagram of this material. Moreover, as documented in many pyrochlore compounds such as $Tb_2Ti_2O_7$ [15], $Er_2Ti_2O_7$ [16], or $Yb_2Ti_2O_7$ [17], weak substitution, often less than 5%, can change the physical properties leading to a quick collapse of the ground state. With this in view, the study was extended to the $Nd_2(Zr_{1-x}Ti_x)_2O_7$ family, using two nominal compositions $x = 0.025$ and $x = 0.1$. These investigations yield a systematic and comprehensive survey of the (H, T) phase diagram for magnetic fields applied along the three main high-symmetry directions ([001], [110], and [111]) of the pyrochlore lattice.

The paper is organized as follows. In Sec. II, we introduce the main properties of $Nd_2Zr_2O_7$ and the context of the study.

*melanie.leger@neel.cnrs.fr
†elsa.lhotel@neel.cnrs.fr
‡sylvain.petit@cea.fr

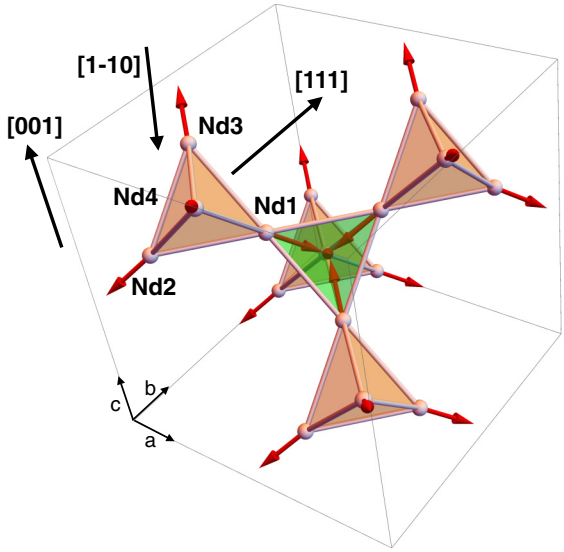

FIG. 1. Sketch of one configuration of the AIAO ordered state of the Nd pyrochlore lattice in the unit cell of $Nd_2Zr_2O_7$. By convention, outer tetrahedra are red, while the central tetrahedron is green. Note that to avoid any confusion between the so-called all in/all out magnetic structure, and the possible magnetic domains associated to this state, we use different notations for the state (AIAO) and for the domains ($\overline{\text{AIAO}}$ or $\overline{\text{AOAI}}$). The depicted configuration, with red all out tetrahedra and green all in tetrahedron, is labeled $\overline{\text{AOAI}}$. The other configuration, $\overline{\text{AIAO}}$, would have red all in tetrahedra and green all out tetrahedron. The figure also features the Nd^{3+} ions labeled according to Table I.

In Secs. III and IV, we present the experimental methods and determination of the (H, T) phase diagrams for the three studied samples and the three field directions. Finally, by comparing these results with mean field (MF) calculations, we discuss in Sec. V the involved field-induced processes, including the role of domains and metastable states, and address the impact of Ti substitution on the phase diagram.

II. EXPERIMENTAL BACKGROUND AND INTERPRETATIONS: A SHORT REVIEW

Using a combination of magnetization, elastic, and inelastic neutron scattering measurements [9,11], previous investigations of $Nd_2Zr_2O_7$ have shown that the Nd^{3+} magnetic moments exhibit a strong Ising anisotropy along local $\langle 111\rangle$ axes, together with a dipolar-octupolar nature [18], different from the standard Kramers doublets studied so far. Furthermore, neutron diffraction has shown that the AIAO antiferromagnetic state (Fig. 1) is characterized by a strongly reduced ordered moment [9,10,19], and coexists with a pinch point pattern typical of spin ice. Nevertheless, inelastic neutron scattering clearly pointed out that, at low temperature, this pattern is not an elastic feature as in classical spin ice, yet is dynamic, shifted to finite energy by an energy $E_o \approx 70\ \mu$eV, and that was hence called a dynamical spin ice mode [11]. In other terms, the peculiar AIAO order of $Nd_2Zr_2O_7$ appears to be protected by a gap E_o from spin ice. In addition, the spin excitation spectrum revealed by inelastic neutron scattering also encompasses well-resolved dispersing features akin to spin-wave branches. These experimental results suggest that quantum effects are at play.

TABLE I. Sign convention used in the FULLPROF refinements. Atoms listed as Nd1 to Nd4 (with (X, Y, Z) positions) form the outer tetrahedron sketched in red in Fig. 1. With this convention, positive values of the magnetic moments correspond to outgoing spins, parallel to the Ising vector $\mathbf{z} = (n_x, n_y, n_z)$. The 12 other atoms are obtained by symmetry operations.

Nd atoms	X	Y	Z	n_x	n_y	n_z
Nd1	0.25	0.25	0.50	1	1	−1
Nd2	0.00	0.00	0.50	−1	−1	−1
Nd3	0.00	0.25	0.75	−1	1	1
Nd4	0.25	0.00	0.75	1	−1	1

Concomitantly, theoretical studies highlighting the dipolar-octupolar nature of the Nd^{3+} ion [18] have shown that the relevant variable is a pseudospin τ_i ($i = x, y, z$ defined in the local ion frame) which resides on the pyrochlore lattice sites. The magnetic moment $\mathbf{J}$, hence the observable quantity, essentially identifies with the τ_i^z component of this pseudospin and is carried by the local $\mathbf{z} = \langle 111\rangle$ axes, consistent with the observed Ising nature of the Nd^{3+} ion. The x and y components identify with octupolar moments of the $4f$ electronic distribution and are thus barely visible to neutrons [20], but importantly the x component transforms like a dipole and thus can be coupled to the z component. The low-energy properties are then governed by

$$\mathcal{H} = \sum_{\langle i,j\rangle} \left[\mathrm{J}_x \tau_i^x \tau_j^x + \mathrm{J}_y \tau_i^y \tau_j^y + \mathrm{J}_z \tau_i^z \tau_j^z + \mathrm{J}_{xz} \left(\tau_i^x \tau_j^z + \tau_i^z \tau_j^x \right) \right],$$

which, after a rotation in spin space by an angle θ, can be recast in the XYZ Hamiltonian [12,18],

$$\begin{aligned} \mathcal{H} &= \sum_{\langle i,j\rangle} \left[\tilde{\mathrm{J}}_{\tilde{x}} \tau_i^{\tilde{x}} \tau_j^{\tilde{x}} + \tilde{\mathrm{J}}_{\tilde{y}} \tau_i^{\tilde{y}} \tau_j^{\tilde{y}} + \tilde{\mathrm{J}}_{\tilde{z}} \tau_i^{\tilde{z}} \tau_j^{\tilde{z}} \right] \\ \text{with} \quad \tilde{\mathrm{J}}_{\tilde{x}} &= \frac{1}{2} \left(\mathrm{J}_x + \mathrm{J}_z + \sqrt{(\mathrm{J}_x - \mathrm{J}_z)^2 + 4\mathrm{J}_{xz}^2} \right), \\ \tilde{\mathrm{J}}_{\tilde{z}} &= \frac{1}{2} \left(\mathrm{J}_x + \mathrm{J}_z - \sqrt{(\mathrm{J}_x - \mathrm{J}_z)^2 + 4\mathrm{J}_{xz}^2} \right), \\ \tan 2\theta &= \frac{2\mathrm{J}_{xz}}{\mathrm{J}_x - \mathrm{J}_z}, \end{aligned} \tag{1}$$

and where the rotation away from the $\mathbf{z}$ axis defines the new components $(\tau^{\tilde{x}}, \tau^{\tilde{y}}, \tau^{\tilde{z}})$ and the new coupling constants $(\tilde{\mathrm{J}}_{\tilde{x}}, \tilde{\mathrm{J}}_{\tilde{y}}, \tilde{\mathrm{J}}_{\tilde{z}})$. According to the most recent investigations [14,21], the parameters yielding an accurate description of the spin dynamics are $\tilde{\mathrm{J}}_{\tilde{x}} \simeq 1$, $\tilde{\mathrm{J}}_{\tilde{z}} \simeq -0.5$ K and $\tilde{\mathrm{J}}_{\tilde{y}}$ close to zero. The corresponding ground state is an AIAO state with the magnetic moments aligned along the $\tilde{\mathbf{z}}$ directions, as proposed in Ref. [12]. It is worth noting that the ordered pseudospin is close to its full value 1/2. The tilted angle $\theta = 1 - 1.2$ rad is estimated from the Curie-Weiss temperature or from the observed ordered moment. Indeed, the projection of the $\tilde{\mathbf{z}}$-ordered moment back to the original $\mathbf{z}$ axes introduces a factor of $\cos\theta$, hence providing a simple explanation for the experimental observation of an AIAO state with a reduced magnetic moment.

TABLE II. Sample (single crystals) parameters obtained from the structural and magnetic FULLPROF refinements at 6 K and from magnetization measurements. The results from the refinements are averaged over the three sets of measurements corresponding to different scattering planes.

Single crystal sample	Ti concentration [%]	O(48*f*) position	Lattice parameter [Å]	T_N [mK]	θ_{CW} [mK]	μ_{eff} [μ_B]	Ordered moment [μ_B]
$Nd_2Zr_2O_7$	0	0.337 ± 0.002	10.66 ± 0.02	285	195	2.45	0.8 ± 0.05
$Nd_2Zr_{1.95}Ti_{0.05}O_7$	2.41 ± 0.2	0.336 ± 0.001	10.65 ± 0.02	375	235	2.52	1.19 ± 0.03
$Nd_2Zr_{1.8}Ti_{0.2}O_7$	7.9 ± 0.7	0.336 ± 0.001	10.64 ± 0.03	325	220	2.50	1.06 ± 0.04

In this paper, we combine neutron diffraction and magnetization measurements to explore the evolution of the AIAO magnetic configuration as a function of temperature and magnetic field **H** applied along the three high-symmetry directions and in the presence of nonmagnetic Ti substitution at the B site of the pyrochlore lattice. This study thus envisages the effect of a Zeeman term added to the XYZ Hamiltonian of Eq. (1):

$$\mathcal{H}_Z = \sum_i -g_z \mu_B \, \tau^{\mathbf{z}}{}_i . \mathbf{H}$$
$$= \sum_i -g_z \mu_B \left[\cos\theta \tau_i^{\tilde{z}} + \sin\theta \tau_i^{\tilde{x}}\right](\mathbf{z}_i . \mathbf{H}). \qquad (2)$$

$\mathbf{z}_i$ are the local $\langle 111 \rangle$ directions and g_z is the anisotropic g factor, estimated to be 4.8 in the pure compound and 5 in the 2.5 and 10% Ti-substituted samples. In addition to classical parameters like effective moment, Curie-Weiss and Néel temperatures, the detailed analysis of the M versus H curves highlights significant field-induced processes, like metamagnetic transitions, that are further analyzed by means of neutron diffraction. This methodology allows one to determine in a systematic way how the microscopic magnetic structure evolution is related to the changes that occur at a more macroscopic scale.

It is worth noting that, as described above, the measured ordered component in zero field is only a fraction of the total magnetic moment of the Nd^{3+} ion ($2.4 - 2.5\,\mu_B$) (see Table II). Nevertheless, in the presence of a magnetic field, the pseudospins tilt toward the local **z** directions, so the measured ordered moment (which is only the **z** component) recovered in high field corresponds to the total magnetic moment.

III. METHODS

A. Samples

$Nd_2(Zr_{1-x}Ti_x)_2O_7$ samples (with $x = 0.025$ and 0.1) were prepared at the University of Warwick in polycrystalline form by standard solid-state chemistry methods, using Nd_2O_3, ZrO_2, and TiO_2 as starting reagents [22,23]. To ensure the appropriate composition of the final compounds, the Nd_2O_3 powder was preheated in air at 1000 °C for 24 h. Powders of the starting oxides were weighed in stoichiometric amounts, mixed together, pressed into pellets, and then heat treated in air for several days (in three or fours steps) at temperatures in the range $1400 - 1500$ °C. The annealed pellets were reground between each step of the synthesis to ensure good homogeneity and to facilitate the chemical reaction. Powder x-ray diffraction measurements confirmed the phase purity of the synthesized $Nd_2(Zr_{1-x}Ti_x)_2O_7$ polycrystalline samples.

Single crystals of the two Ti-substituted samples were grown from the polycrystalline samples by the floating-zone technique using a four-mirror xenon arc lamp optical image furnace [22,23]. The 2.5% substituted sample is a fragment of the single crystal used in Ref. [14].

The pure sample is the same as in Refs. [9,11].

Below, we report only on the single crystal properties. Powder sample properties are summarized in Appendix B.

B. Bulk magnetic measurements

Magnetization and AC susceptibility measurements were performed down to 80 mK on the single crystal samples using superconducting quantum interference device magnetometers, equipped with a dilution refrigerator developed at the Institut Néel-CNRS Grenoble [24]. The crystals were glued with GE varnish on a copper plate and measurements were collected with the magnetic field aligned along the three high-symmetry directions of the crystals ([111], [1$\bar{1}$0], or [001]). All the data shown below were corrected from demagnetizing field effects. Demagnetizing factors were estimated from the sample shapes using the Aharoni formula [25].

C. Neutron diffraction

Single crystal diffraction experiments were carried out at D23 (CRG CEA-ILL, France) using a wavelength $\lambda = 1.275$ Å and operated with a copper monochromator. The samples were glued on the Cu finger of a dilution insert and placed in a cryomagnet. The experiments were conducted with the (vertical) field **H** either parallel to the [001], [1$\bar{1}$0], or [111] high symmetry crystallographic direction. The three orientations were measured for the three samples, except for the 10% substituted sample for which the $\mathbf{H} \parallel [1\bar{1}0]$ condition could not be measured.

As we shall see later, the magnetic structures have a $\mathbf{K} = \mathbf{0}$ propagation vector, hence magnetic and crystalline intensities occur on the same (h, k, l) positions. A full data collection was thus first measured at 6 K to serve as a reference of the crystalline intensities and refine the sample volume, the Ti content x, the extinction parameters, and atomic positions in the $Fd\bar{3}m$ space group. Additional data collections (consisting of 80 Bragg peaks) were then measured at low temperature (60 mK), at selected fields ranging from -1 T to $+1$ T. The magnetic structure at each field was then refined with the FULLPROF suite [26] using the difference between the low temperature and 6 K diffractogram intensities. Owing to the strong Ising character of the Nd^{3+} ions, the data have been analyzed assuming that the magnetic moments lie along the **z**

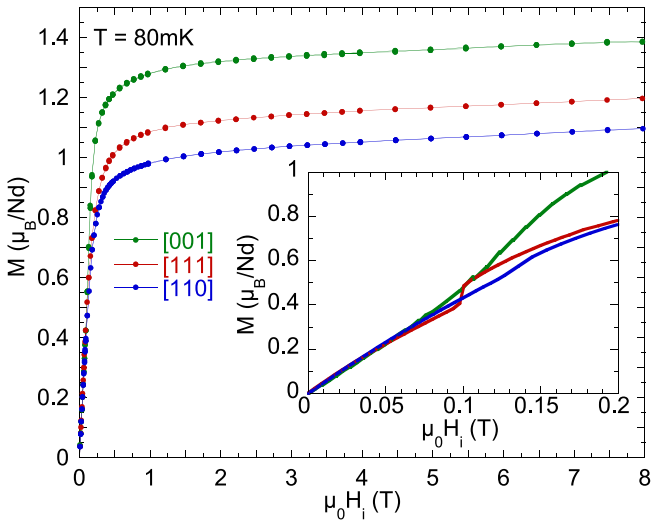

FIG. 2. Magnetization M versus internal field H_i measured with the field applied along the three main high-symmetry directions at 80 mK on the 10%-Ti substituted sample $Nd_2Zr_{1.8}Ti_{0.2}O_7$. Similar curves are observed in the 2.5%-Ti substituted sample. Inset: Zoom in of the low field data.

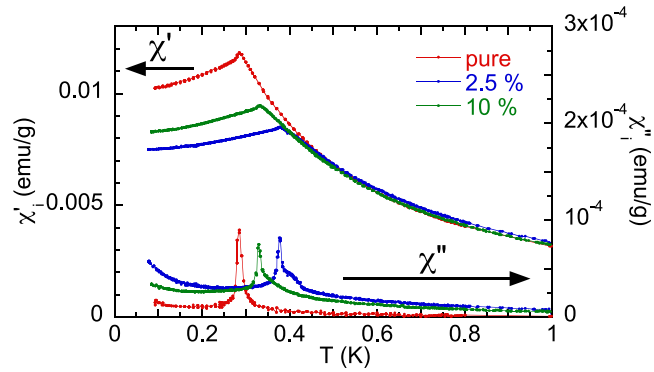

FIG. 3. Real and imaginary parts of the AC susceptibility χ' (left) and χ'' (right) for the pure (red dots), 2.5% (blue dots), and 10% (green dots) substituted samples, along the $[1\bar{1}0]$ direction. Measurements were performed with $H_{AC} = 2.7$ Oe and a frequency $f = 5.7$ Hz.

Ising axes (see Table I). The sign, with respect to the convention given in Table I and the amplitude of the moments in a given tetrahedron are the free parameters of those fits.

In addition, the intensity of selected Bragg peaks was recorded while ramping the field back and forth from -1 T to $+1$ T (0.015 T/min was the minimum sweeping speed) to obtain a continuous evolution versus field. The sample was first cooled down to 60 mK in zero field and the field dependence of the intensity was then measured after the application of a $+1$ T field to saturate the sample (larger fields up to $+3$ T were also used but this makes no changes in the low field results). The detailed method for the analysis of these field-sweeping measurements is given in Appendix C.

IV. RESULTS

A. Physical characterizations

The structural refinements from neutron diffraction data of the single crystals with the 2.5 and 10% substitution concentrations are in agreement with the pyrochlore structure. The lattice parameters are close to the pure compound one (10.66 Å) and the 48*f* oxygen atoms are found at the position $x_{48f} = 0.336$. Note that the value of the Ti content was refined thanks to the significant difference in the scattering length for the two elements Zr and Ti. It is found to be 2.4 and 7.9% in the so-called 2.5 and 10% Ti-substituted samples, respectively (see Table II).

Isothermal magnetization curves for magnetic fields applied along the three high-symmetry directions show three different saturated magnetizations (see Fig. 2), in agreement with expectations in the case of ⟨111⟩ Ising spins located at the vertices of the tetrahedra [27]. Curie-Weiss fits of the magnetization between 1 and 4 K give positive Curie-Weiss temperatures θ_{CW} and effective moments of about 2.5 μ_B for both Ti-substituted samples.

AC susceptibility measurements show a transition at low temperature in all compounds with a peak in both real and imaginary parts (see Fig. 3). No frequency dependence of the peak position is observed between 0.057 and 570 Hz. Interestingly, the critical temperature T_N reaches 376 mK for $x = 2.5\%$ and decreases back to 325 mK for $x = 10\%$. Neutron diffraction measurements elucidate that the magnetic ground state is AIAO in the substituted samples with 1.2 and 1.1 μ_B for the 2.5 and 10% substituted samples, respectively. For both samples, the transition takes place at a higher temperature than in the pure compound ($T_N = 285$ mK) and with an ordered magnetic moment significantly larger (0.8 μ_B in the pure compound), as summarized in Table II. It should be noted that these T_N and ordered moment values for the substituted samples are nevertheless smaller than the ones measured on the powder samples with the same composition (see Appendix B).

At low field and in all samples, the M versus H curves show an inflexion point (see the insert in Fig. 2) for the three field directions, which is associated to metamagneticlike processes [9]. The corresponding characteristic field can be followed by tracking the maximum of the derivative dM/dH_i versus H_i of these magnetization curves for different temperatures to build the (H, T) phase diagram. In the following sections, the nature of the phases is investigated based on neutron diffraction data.

B. Magnetic field along [001]

When applying a magnetic field along the [001] direction, the AIAO ground state is expected to evolve toward an ordered spin ice state, with two incoming and two outgoing spins per tetrahedron and a net magnetization along the [001] direction. According to symmetry, the four spins in a given tetrahedron form two subgroups consisting of spins (1,2) and (3,4) (see Fig. 1). To follow the magnetic structure and figure out how the ordered spin ice configuration grows to the detriment of the AIAO one, it is thus convenient to parametrize the magnetic moments as

$$\mathbf{m}_1 = (m_{AIAO} - m_{2I2O})\,\mathbf{z}_1 = x\,\mathbf{z}_1,$$
$$\mathbf{m}_2 = (m_{AIAO} - m_{2I2O})\,\mathbf{z}_2 = x\,\mathbf{z}_2,$$

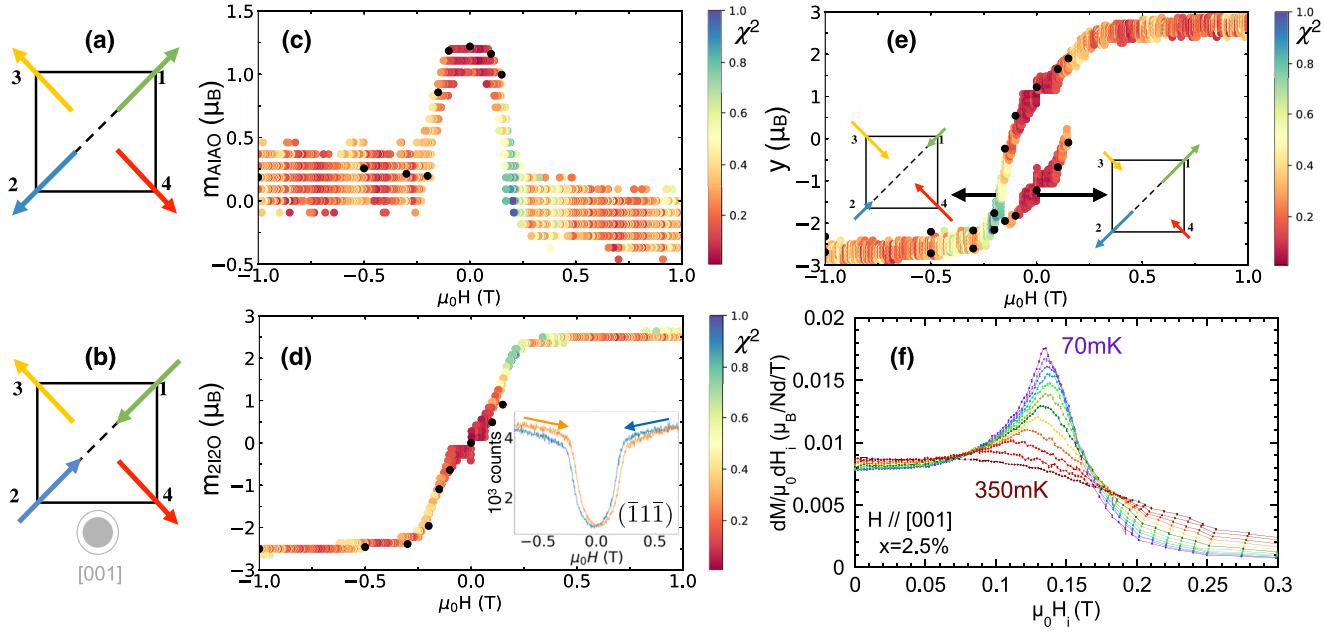

FIG. 4. Field dependence for **H** ∥ [001] in the 2.5%-substituted sample. (a) Sketch of the four spins in the all out state, obtained in zero field and (b) of the 2I2O state obtained at saturation. (c)–(e) Neutron diffraction results: (c) m_{AIAO}, (d) m_{2I2O}, and (e) total y component versus H [see Eq. (3)]. The left (respectively, right) branch results from $m_{AIAO} > 0$—all out component ($m_{AIAO} < 0$—all in component). FULLPROF refinements are displayed as full black dots. Colored points indicate the most probable values obtained from the field-sweeping measurement analysis (see Appendix C). The color scale indicates the χ^2 value obtained from Eq. (C1). The inset of (d) shows the intensity of the $(\bar{1}1\bar{1})$ reflection. (f) dM/dH_i versus H_i. The field was always swept from negative to positive values.

$$\mathbf{m}_3 = (m_{AIAO} + m_{2I2O})\,\mathbf{z}_3 = y\,\mathbf{z}_3,$$
$$\mathbf{m}_4 = (m_{AIAO} + m_{2I2O})\,\mathbf{z}_4 = y\,\mathbf{z}_4, \qquad (3)$$

which corresponds to the sum of a generalized all in/all out component m_{AIAO} and of a two in-two out component m_{2I2O}. By convention, considering a red tetrahedron of Fig. 1, m_{AIAO} is positive (negative) when all the Nd magnetic moments are out (in), and m_{2I2O} is positive when Nd1 and Nd2 are in, while Nd3 and Nd4 are out (2I2O configuration) and negative when Nd1 and Nd2 are out while Nd3 and Nd4 are in (2O2I configuration).

The FULLPROF refinements highlight this field-induced behavior, as shown in Fig. 4 for the 2.5% substituted sample. Starting from $\mu_0 H = -1$ T, red tetrahedra of Fig. 1 are in the 2O2I configuration with a net moment along [00-1]. Upon increasing field, this two in-two out component remains stable (decreasing smoothly) up to a field threshold from which it is suppressed to the benefit of the AIAO component, as shown in Figs. 4(c) and 4(d). This characteristic field is clearly observed when measuring the intensity of the $(\bar{1}1\bar{1})$ reflection as a function of field, as shown in the inset of Fig. 4(d).

The AIAO component is maximum in zero field. It decreases when further increasing the field, while m_{2I2O} rises continuously until reaching a value close to the saturation at the opposite of the first threshold field, i.e., when the AIAO component comes back to zero. This clearly separates two regions in the phase diagram: above a characteristic field H_{001}, only a 2I2O component is present, while below it coexists with an AIAO one.

The analysis nevertheless points to two different situations upon increasing field from the 2O2I configuration: (i) either Nd1 and Nd2 flip, so the Fig. 1 red tetrahedra become all in (and green tetrahedra become all out) or (ii) Nd3 and Nd4 flip, so the red tetrahedra become all out. These two magnetization processes lead to the formation of the two domains of the AIAO state, so-called $\overline{\text{AIAO}}$ or $\overline{\text{AOAI}}$ (see Fig. 5), which cannot be distinguished in neutron diffraction measurements. The two domains have the same energy in the presence of the [001] field, which suggests that both are present simultaneously. Interestingly, the resulting moment [x or y in Eq. (3)] on a given atom is different depending on the sign of m_{AIAO}, and thus on which AIAO domain is stabilized. This manifests through the two branches shown in Fig. 4(e) representing the magnetic moment of the Nd3 atom. Finally, almost no hysteresis is observed in magnetization and neutron field-sweeping measurements, which indicates that

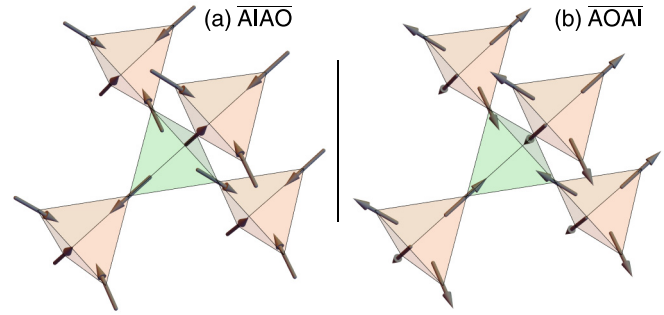

FIG. 5. Pictures of the two domains of the AIAO state. (a) $\overline{\text{AIAO}}$ domain: Red tetrahedra are all in and green tetrahedra are all out. (b) $\overline{\text{AOAI}}$ domain: Red tetrahedra are all out and green tetrahedra are all in.

TABLE III. Critical fields at the lowest temperature for the three high-symmetry directions, obtained experimentally for the three samples, and by mean-field calculations for the pure and 2.5% samples.

Sample	$\mu_0 H_{001}$ (T)	$\mu_0 H_{110}$ (T)	$\mu_0 H_{111}$ (T)
Experiments			
Pure	0.083	0.086	0.075
2.5%	0.135	0.162	0.111
10%	0.124	0.132	0.099
Calculations			
Pure	0.26	0.55	1.20
2.5%	0.32	0.72	1.13

both domains are present and that the magnetization process takes place while remaining close to thermodynamic equilibrium.

The signature of H_{001} in the magnetization curves versus field is an inflexion point, which appears as a broad peak in the dM/dH_i versus field curves [see Fig. 4(f)]. At the lowest temperature (about 80 mK), H_{001}, determined from the maximum of dM/dH_i, varies from 0.08 up to 0.135 T depending on the sample composition (see Table III). The values of H_{001} as a function of temperature are plotted for the three samples on the (H, T) phase diagram of Fig. 8(a). As expected, H_{001} goes to zero at the Néel temperature, confirming that it is characteristic of the disappearance of the AIAO structure. The temperature dependence of H_{001} is qualitatively similar in the three samples. Interestingly, the lower the T_N, the lower the H_{001}. Consequently, the pure compound has the lowest H_{001} and the 2.5% Ti-substituted sample has the highest one.

C. Magnetic field along [1$\bar{1}$0]

In the presence of a [1$\bar{1}$0] field, the situation is more complicated. In such a field direction, the system is usually described as two perpendicular chains, made of spins 1 and 2 (β chains), and spins 3 and 4, respectively, in our notations (α chain, see Fig. 1). Spins 3 and 4 are almost collinear to the field and are thus expected to quickly reach saturation. In contrast, spins 1 and 2 have their Ising direction perpendicular to the field. The Zeeman effect is thus zero, yet the field indirectly affects their orientation via the coupling to the other spins [27]. To describe the magnetic structure as a function of field, the following parametrization was thus used:

$$\begin{aligned}
\mathbf{m}_1 &= (m_{\mathrm{AIAO}} + m_\perp)\,\mathbf{z}_1,\\
\mathbf{m}_2 &= (m_{\mathrm{AIAO}} - m_\perp)\,\mathbf{z}_2,\\
\mathbf{m}_3 &= (m_{\mathrm{AIAO}} + m_\parallel)\,\mathbf{z}_3,\\
\mathbf{m}_4 &= (m_{\mathrm{AIAO}} - m_\parallel)\,\mathbf{z}_4.
\end{aligned} \tag{4}$$

It takes into account the AIAO contribution m_{AIAO} (with the same sign convention as before) along with $m_\parallel$ and $m_\perp$, which feature field-polarized components parallel (for spins 3 and 4) and perpendicular to the nominal field direction (for spins 1 and 2).

FULLPROF refinements of the neutron diffraction measurements highlight the saturation of the parallel spins in large magnetic fields: at $|\mu_0 H| = 1$ T, the Nd3 and Nd4 moments reach $2.4 - 2.5\,\mu_B$, the Nd3 moment being in, and the Nd4 one out in positive field [see Fig. 6(b)], and conversely in negative field. Note that they reach values as high as $1.5\,\mu_B$ at $|\mu_0 H| = 0.15$ T [see Fig. 6(d)]. At high field, the refined magnetic moment on sites 1 and 2 is found to be zero (or small [28]) [see Fig. 6(c)]. This confirms the disordered character of the (Nd1, Nd2) chains in applied field previously observed in Ref. [29]. This paper further reports diffuse scattering showing the existence of short-range correlations within the β chains, that we could not address in the present paper.

Neutron refinements [see Fig. 6(c)] show that the AIAO component is suppressed upon increasing the field (in absolute values) at a critical value labeled H_{110}. It is best observed when measuring the characteristic (1$\bar{1}$3) magnetic reflection as a function of the field, as shown in the inset of Fig. 6(c).

Like in the case of the [001] field, the analysis of the field-sweeping measurements unveils two scenarios regarding the rise of the AIAO component when starting from the high field state, and corresponding to the possible $\overline{\mathrm{AIAO}}$ and $\overline{\mathrm{AOAI}}$ domains. Indeed, considering the (Nd3, Nd4) α chain in the saturated state, either the Nd3 or the Nd4 spin can flip to recover AIAO configurations, with the same energy cost. It results in two possible branches in the total magnetic moment, as shown for the Nd3 atom in Fig. 6(e).

The signature of H_{110} in the magnetization curves versus field is characterized by a steplike anomaly and manifests as a little peak in the dM/dH_i curves [see Fig. 6(f)], which is more marked in the substituted samples than in the pure sample. Nevertheless, this peak is only clearly observed in the positive field, when sweeping the field from negative values, as shown in the inset of Fig. 6(f) at 70 mK. A small irreversibility is also observed on the (220) reflection (not shown) in neutron diffraction measurements. These results imply that some kind of metastable states exist for this field direction, which we will address in more details in the discussion. The temperature dependence of H_{110} is qualitatively similar in the three samples and, as for the [001] direction, the pure compound has the lowest H_{110} while the 2.5% Ti-substituted sample has the highest one.

D. Magnetic field along [111]

To discuss the case of a field applied along the [111] direction, it is convenient to view the pyrochlore lattice as the stacking of triangular and kagomé planes. In a given tetrahedron, one shall then distinguish the apex spin, which is collinear to the field (Nd2), and three kagomé spins located in the kagomé layer (Nd1, 3, and 4), which experience the same Zeeman effect. The magnetic configuration is expected to go from a 1O3I to all in or all out, and eventually to 1I3O with increasing the field from -1 up to $+1$ T, a behavior described in the pure compound in Refs. [19,30]. To describe this evolution, the following parametrization is used:

$$\begin{aligned}
\mathbf{m}_1 &= m_{\mathrm{kagome}}\,\mathbf{z}_1,\\
\mathbf{m}_2 &= m_{\mathrm{apex}}\,\mathbf{z}_2,\\
\mathbf{m}_3 &= m_{\mathrm{kagome}}\,\mathbf{z}_3,\\
\mathbf{m}_4 &= m_{\mathrm{kagome}}\,\mathbf{z}_4.
\end{aligned} \tag{5}$$

Neutron diffraction refinements reveal in both Ti-substituted samples the same singularity as the one already observed in

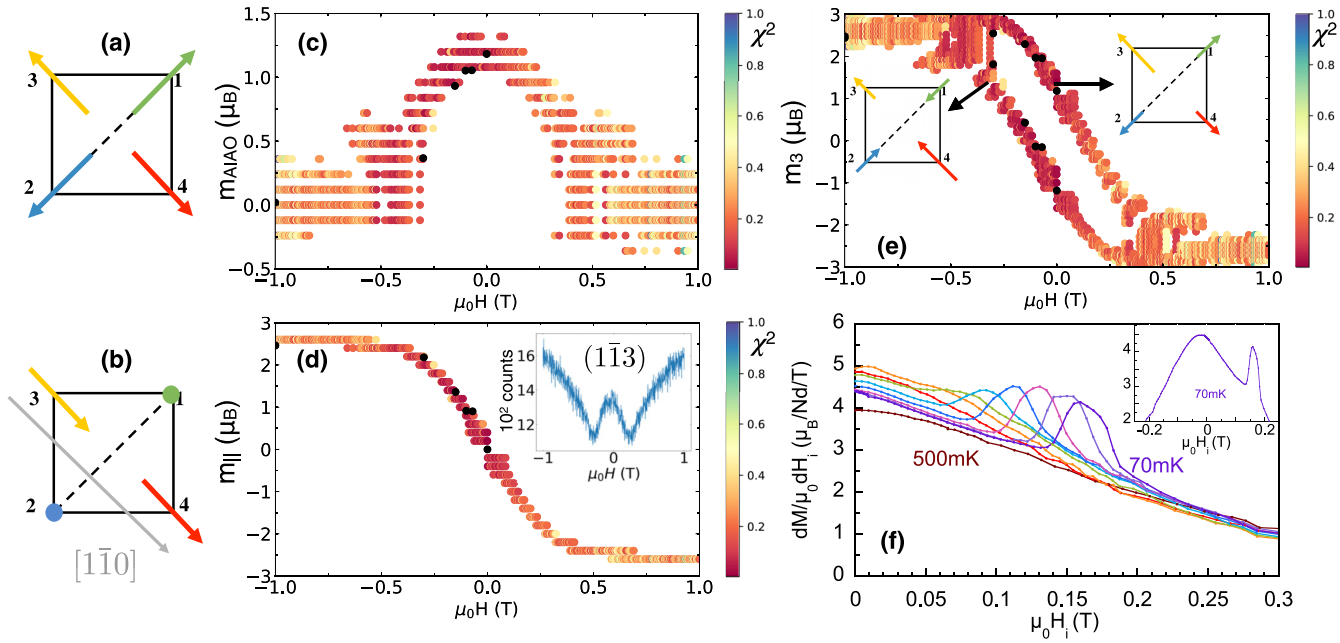

FIG. 6. Field dependence for **H** ∥ [1$\bar{1}$0] in the 2.5%-substituted sample. (a) Sketch of the four spins in the all out state, obtained in zero field and (b) of the partially ordered state obtained at saturation. (c)–(e) Neutron diffraction results: (c) m_{AIAO}, (d) $m_{\parallel}$, and (e) total m_3 component versus H [see Eq. (4)]. The right (respectively, left) branch results from $m_{\mathrm{AIAO}} > 0$—all out component ($m_{\mathrm{AIAO}} < 0$—all in component). FULLPROF refinements are displayed as full black dots. Colored points indicate the most probable values obtained from the field-sweeping measurements analysis (the color scale corresponds to the χ^2 value, see Appendix C). The inset of (d) shows the intensity of the $(1\bar{1}3)$ reflection. (f) dM/dH_i versus H_i at different temperatures between 70 and 500 mK. The inset shows the whole curve at 70 mK. The field was always swept from negative to positive values.

the pure compound. It is characterized by a sudden jump for both the apex and the kagomé spins [see Figs. 7(c) and 7(d)]. At $\mu_0 H = -1$ T, the kagomé spins are in while the apex is out, forming a 1O3I configuration. Upon increasing the field from -1 T, the absolute value of the apex moment progressively decreases while the kagomé moments remain essentially unchanged. At some threshold $\mu_0 H \approx -0.02$ T, the apex moment changes signs, and the structure becomes all in. This holds up to a critical field $\mu_0 H_{111} \approx 0.1$ T where the kagomé moments abruptly flip while the apex moment nearly goes back to zero. Its amplitude increases then but now follows a new magnetization process. The configuration has become 1I3O. The H_{111} field is best observed when measuring the characteristic $(\bar{1}\bar{3}1)$ magnetic reflection as a function of the field, as shown in Fig. 7(e).

The sharp transition at H_{111} underlines the existence of metastable states when increasing the field, and which are again connected to the formation of either all in or all out configurations for the red tetrahedra, and thus to $\overline{\mathrm{AIAO}}$ and $\overline{\mathrm{AOAI}}$ domains. These domains are connected to the $\overline{\mathrm{1O3I/1I3O}}$ and $\overline{\mathrm{1I3O/1O3I}}$ configurations stabilized at large negative and positive fields, respectively. Depending on the amplitude of the field, they become metastable, explaining the origin of the hysteresis clearly observed in the magnetization measurements displayed in the inset of Fig. 7(f).

E. Phase diagrams

From the temperature dependence of the peak in the dM/dH_i versus H_i curves shown in Figs. 4(f), 6(f), and 7(f), we could construct the phase diagrams for the three field directions and the three measured samples. They are displayed in Fig. 8. The three samples show qualitatively the same behavior, the critical fields being related to the critical temperatures in all directions so the larger the Néel temperature, the larger the critical field.

Along the [001] and [1$\bar{1}$0] directions, the low field phase can be directly associated to an AIAO phase, as demonstrated by the neutron diffraction results detailed in the above sections. Along [001], the critical fields seem to saturate at low temperature (and even to decrease slightly for the 2.5% sample). On the contrary, the low-temperature dependence of the critical field along [1$\bar{1}$0] does not show any sign of saturation.

The description in terms of AIAO component for the field along the [111] direction is less relevant due to the different responses of the apical and kagomé spins with respect to the field in that case. In addition, the observation of a very strong hysteresis suggests that the value of H_{111} is unlikely an equilibrium value, as discussed in more detail in Sec. V.

To further probe the nature of the field-induced behavior in this field direction, we have performed M versus T measurements in various applied fields. In particular, field cooled (FC) experimental curves are expected to better approach the equilibrium state of the system. Zero field cooled-field cooled (ZFC-FC) experiments were thus conducted at several applied fields between 0 and 1250 Oe for the two substituted samples, as shown in Fig. 9 for the 10% sample. In low field (typically 100 Oe), both ZFC and FC curves show a maximum of the magnetization at a value labeled T_{m}, which occurs roughly

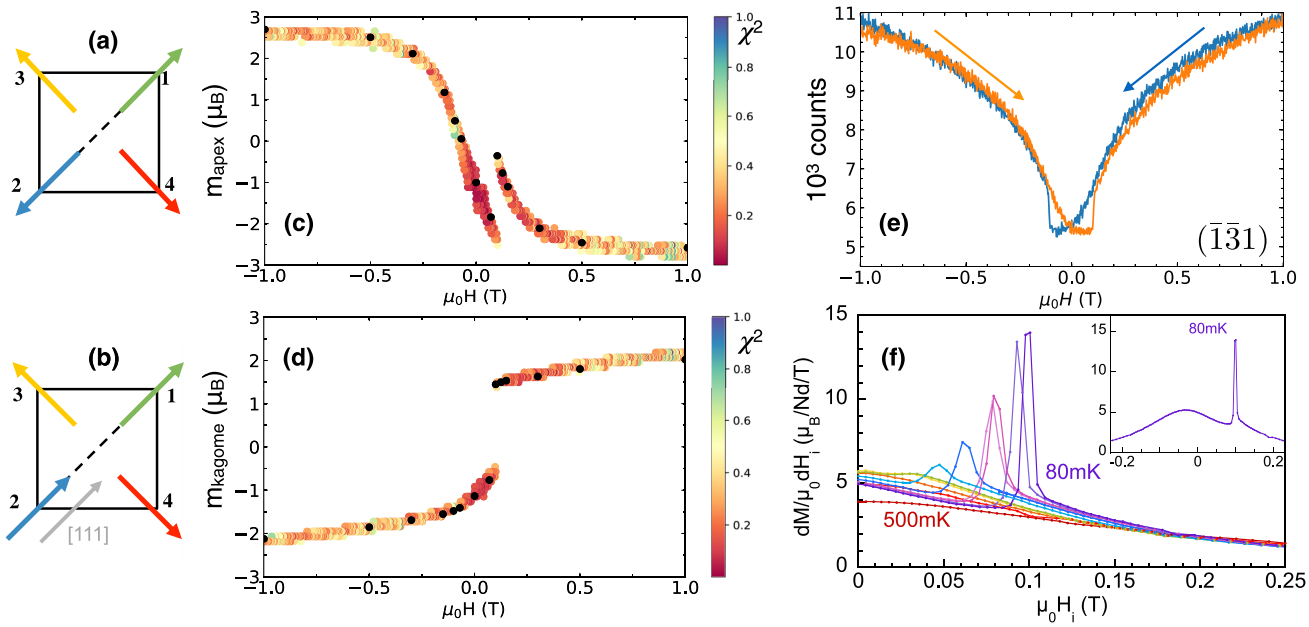

FIG. 7. Field dependence for **H** ∥ [111] in the 10%-substituted sample. (a) Sketch of the four spins in the all out state, obtained in zero field and (b) of the 1I3O state obtained at saturation in a positive field. (c)–(e) Neutron diffraction results: (c) m_{apex} and (d) m_{kagome} components versus H [see Eq. (5)]. FULLPROF refinements are displayed as full black dots. Colored points indicate the most probable values obtained from the field-sweeping measurement analysis (the color scale corresponds to the χ^2 value, see Appendix C). (e) Intensity of the $(\bar{1}\bar{3}1)$ reflection versus H. (f) dM/dH_i versus H_i at different temperatures between 80 and 500 mK. The inset shows the whole curve at 80 mK. The field was always swept from negative to positive values.

at the Néel temperature T_N (determined from the AC susceptibility). However, a splitting between the ZFC and the FC curves is observed at lower temperature, below T_1, with $T_1 < T_m$. As previously observed in the case of $Nd_2Hf_2O_7$ [31], upon increasing the field, this ZFC-FC irreversibility moves to lower temperature, so the ZFC-FC curves remain on top of each other in the temperature range $[T_1, T_m]$.

The obtained characteristic temperatures T_1 and T_m measured at a given applied field are plotted together with the maxima H_1 of dM/dH_i versus H_i measured at constant temperature in the (H, T) phase diagram shown in Fig. 10. Interestingly, the boundary defined by the T_1 points is found to coincide with the H_1 one. Following the diffraction results of Fig. 7, the (T_1, H_1) line thus separates the field-induced one in–three out (or one out–three in) regime (gray shaded region in Fig. 9) and the AIAO low field–low temperature state (blue shaded region in Fig. 9). In the latter, all magnetic moments are oriented in the same way (in or out) along the local **z** directions of a tetrahedron, even if the moment magnitudes are different. Since the FC curve is expected to be an equilibrium curve, T_1 and H_1 would thus correspond to the critical line where the system leaves a metastable state to reach the energetic ground state of the system upon increasing temperature or field. In that picture, the temperature T_m would correspond to the crossover between the field-polarized state and the paramagnetic state. This description, which relies on the knowledge of the magnetic structure thanks to neutron diffraction, differs from the

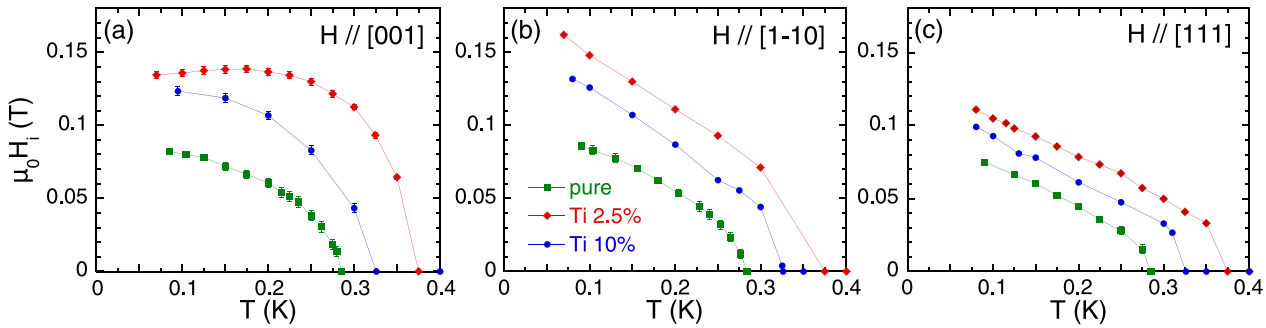

FIG. 8. Field-temperature (H, T) phase diagrams determined from M versus H experiments for the three high-symmetry directions (a) [001], (b) $[1\bar{1}0]$, (c) [111], and for the studied samples: the pure (green squares), the 2.5%-substituted (red diamonds), and the 10%-substituted (blue dots) compounds. Lines are guides to the eye.

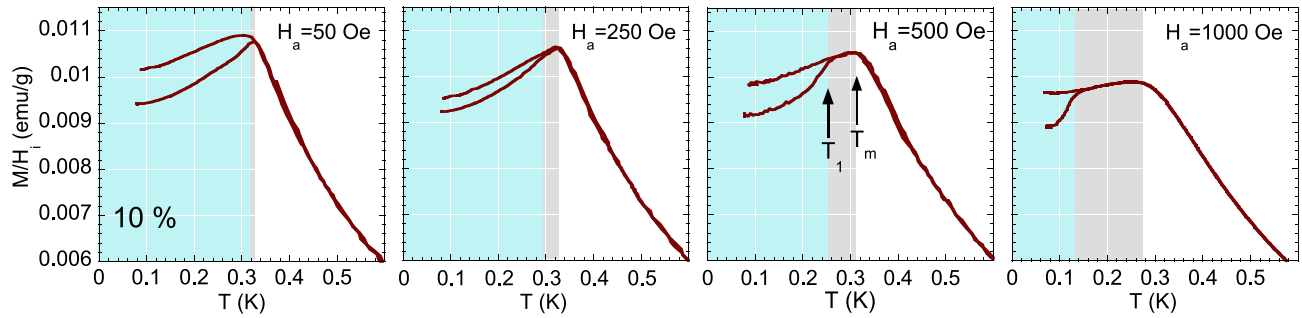

FIG. 9. M/H_i versus temperature for the 10%-Ti substituted sample obtained in ZFC-FC measurements at different applied magnetic fields along [111]. T_1 is defined as the temperature where the ZFC and the FC curves split and T_m is defined as the temperature where M/H_i reaches its maximum.

analysis of Ref. [31] where the gray region was proposed to remain in an AIAO state but with only one domain type. We shall come back to this point in the Discussion.

V. DISCUSSION

A. Analysis of the phase diagrams

The phase diagrams have been calculated in Ref. [21] by Monte Carlo (MC) simulations applied to the XYZ Hamiltonian and using the coupling parameters $(\tilde{J}_{\tilde{x}}, \tilde{J}_{\tilde{y}}, \tilde{J}_{\tilde{z}})$ available for the pure compound (see Fig. 9 of this reference). These calculations were performed applying the field at high temperature and decreasing the temperature, thus corresponding to a FC procedure. Importantly, the so-called ordered parameter in these phase diagrams is associated to the AIAO component relative to the $\tilde{\mathbf{z}}$ directions (defined as $m_{\tilde{z}\ \mathrm{AIAO}} = \frac{1}{N}\sum_i \tilde{\tau}_i^{\tilde{z}}$) and not to the $\mathbf{z}$ components that are actually measured.

We have performed MF calculations with the exchange parameters obtained for the pure compound [14]: $\tilde{J}_{\tilde{x}} = 1.18$, $\tilde{J}_{\tilde{y}} = -0.03$, $\tilde{J}_{\tilde{z}} = -0.53$ K, $\theta = 1.23$ rad [see Eq. (1)]. Those calculations show that for the [001] and [1$\bar{1}$0] field directions, the phase diagrams are identical whether focusing on the $\tilde{\mathbf{z}}$ or $\mathbf{z}$-AIAO component ($m_{z\ \mathrm{AIAO}} = \frac{1}{N}\sum_i \tau_i^z$). This allows one to compare directly the calculated and measured phase diagrams. As previously obtained [21,29], the calculated phase diagrams qualitatively reproduce the observations but the critical fields are smaller in the experiments (see Figs. 8 and 11). In addition, the shape of the transition line for the [1$\bar{1}$0] direction is quite different from the measurements. The zero-field transition temperature is overestimated, as expected for MF calculations.

To clarify the differences between calculations and experiments, we have followed the "energy landscape" approach of Ref. [21]. This consists of finding the configurations which minimize the classical energy, calculated numerically using the XYZ Hamiltonian (see Appendix D). Several solutions can be found, revealing local minima and thus metastable configurations. The corresponding moments are then plotted against the magnetic field, while a color scale is used to keep track of the value of the energy.

Figures 12(a) and 12(b) show the results for the field applied along the [001] direction together with the diffraction results in the pure sample. As expected from a simple symmetry analysis and the neutron results (discussed in Sec. IV B), two magnetic configurations are equivalent in energy and define two branches for the evolution of magnetic moments versus field. This can be seen by plotting the magnetic component y of the Nd3 moment [Fig. 12(a)], or the $m_{z\ \mathrm{AIAO}}$ component [Fig. 12(b)]. Two domains then probably form in the system when ramping the field that cannot be distinguished in experiments. The field value at which the two branches merge, which corresponds to the suppression of the AIAO component, is slightly larger in the calculation than in the experiment but roughly in the same range. The slight hysteresis observed experimentally may be due to a small field misalignment which would favor one domain over the other, resulting in metastable configurations and reducing the critical

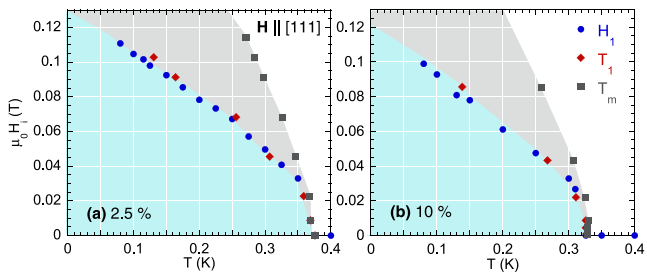

FIG. 10. Phase diagrams (H, T) for $\mathbf{H} \parallel [111]$ from M versus T (T_1, red diamonds, and T_m, green squares) and M versus H (H_1, blue dots) measurements for the 2.5 and 10%-substituted samples.

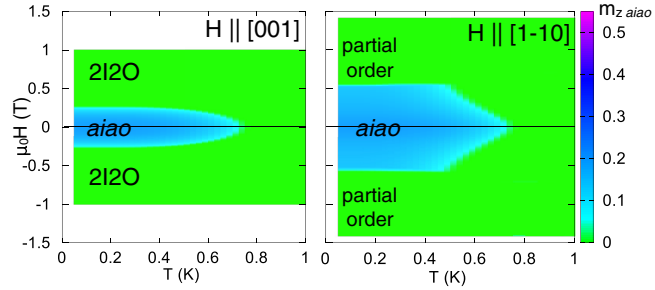

FIG. 11. Mean-field (H, T) phase diagrams calculated for (a) $\mathbf{H} \parallel [001]$ and (b) $\mathbf{H} \parallel [1\bar{1}0]$ for the pure compound parameters. The color scale indicates the value of $m_{z\ \mathrm{AIAO}}$. Phase diagrams were obtained upon decreasing the temperature in FC conditions.

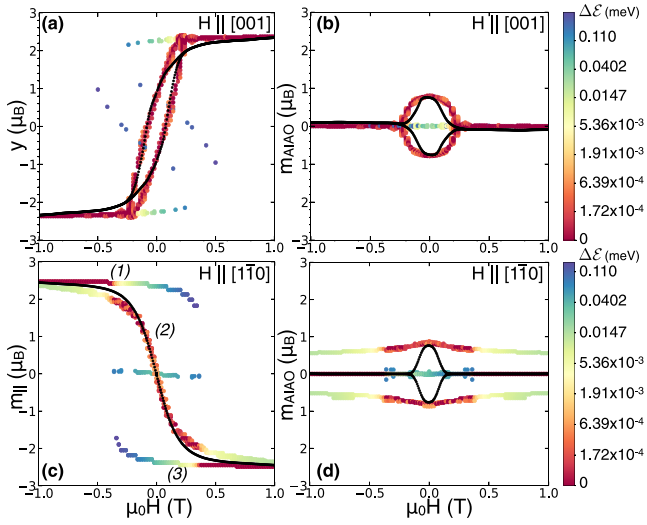

FIG. 12. Magnetic components along **z** as a function of field in the pure sample. (a), (b) **H** ∥ [001]: for (a) $y = m_3$ and (b) m_{AIAO} [see Eq. (3)]. (c), (d) **H** ∥ [1$\bar{1}$0]: for (c) $m_{\parallel}$ and (b) m_{AIAO} [see Eq. (4)]. The color scale represents the energy difference between the calculated configuration and the absolute minimum energy configuration (logarithmic scale), the red color referring to the smallest energy. Black dots correspond to the experimental values obtained from the field-sweeping measurement analysis. Labels (1)–(3) in panel (d) refer to the three branches discussed in the text.

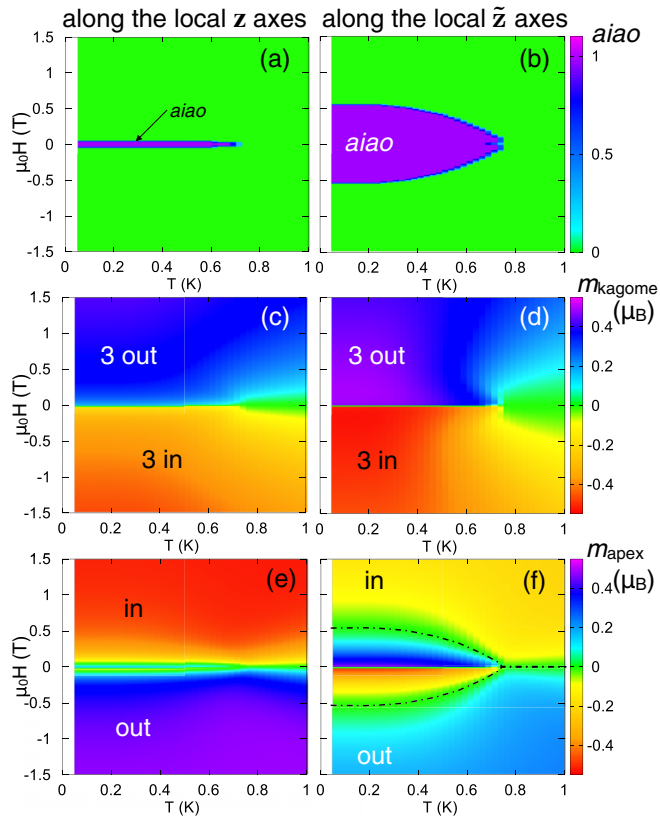

FIG. 13. Mean-field (H, T) phase diagrams obtained for **H** ∥ [111] upon decreasing the temperature in field-cooled conditions for the pure compound parameters. The left and right sides show the same results but projected along the **z** and $\tilde{\mathbf{z}}$ components of the pseudospins, respectively. (a), (b) show the *aiao* parameter (equal to 1 if all the spins are in (or out) and 0 otherwise). (c), (d) display the kagomé spin component m_{kagome}, (e), (f) the apical spin component m_{apex}. Dashed lines are guides to the eye to highlight the region delimited by the *aiao* parameter in (b).

field in a similar way as for the [111] direction that we will discuss below.

In the [1$\bar{1}$0] direction, the agreement between the calculations and the experiments is less convincing as can be seen in Figs. 12(c) and 12(d). The experimental $m_{z\ \mathrm{AIAO}}$ (and thus the two domains) vanishes at much smaller field and more smoothly than in the calculations [Fig. 12(d)] where an abrupt jump is obtained. When focusing on the α chains (Nd3 and Nd4), calculations for the parallel component $m_{\parallel}$ [Fig. 12(d)] predict essentially three branches, labeled (1)–(3) in the figure: branches (1) and (2) correspond to an almost saturated $m_{\parallel}$ moment, and are stable at high values of the (absolute) field. The central branch (3) is stable between about −0.3 and 0.3 T. Looking at the color scale and starting from −1 T, the global energy minimum thus goes from a saturation branch to the other via the central branch. In this part, $m_{z\ \mathrm{AIAO}} \neq 0$ and the moment decreases smoothly. While in the calculations a little step is obtained when going from one branch to the other, concomitantly with the appearance and suppression of the all in or all out component, the experimental data seem to go continuously from one branch to the other.

A small jump is nevertheless observed in the derivative of the magnetization, but it is hysteretic and much weaker than in the present calculations. The discrepancy between the calculations and the experiments may lie in the subtlety of the [1$\bar{1}$0] situation: the two β spins which remain disordered in the nearest neighbor classical approach may be sensitive to octupolar and long range dipolar couplings, or experience order by disorder effects [29,32,33]. It is clear from our results that these ingredients are not strong enough to affect the high field state since the Nd1 and Nd2 moments do not eventually order (which also excludes a strong misalignment of the field), but they may affect the low field picture.

We now turn to the [111] direction, where the description of the field induced process is less direct. Indeed, as already mentioned, the description in terms of an AIAO state is not relevant, due to the different fields felt by the apical and kagomé spins, the main consequence being that all the moments do not have the same length along the field direction. To get a clear insight of what happens in this case, it is convenient to define the *aiao* parameter, which is equal to 1 if all the spins are in (or out) and 0 otherwise. This parameter can have a different value depending on whether it is defined with respect to the $\tilde{\mathbf{z}}$ or to the **z** directions, as illustrated in Figs. 13(a), 13(b), 14(a), and 14(b). Actually, this is of great importance to understand the measured magnetic structure and phase diagrams.

At first, it appears simpler to discuss the phase diagram measured and calculated in FC conditions, since it is expected to describe the equilibrium state and get rid of metastable states. MF calculations shown in Fig. 13 highlight two descriptions. The left column represents the *aiao* parameter and magnetic components along **z**, which can be directly related to

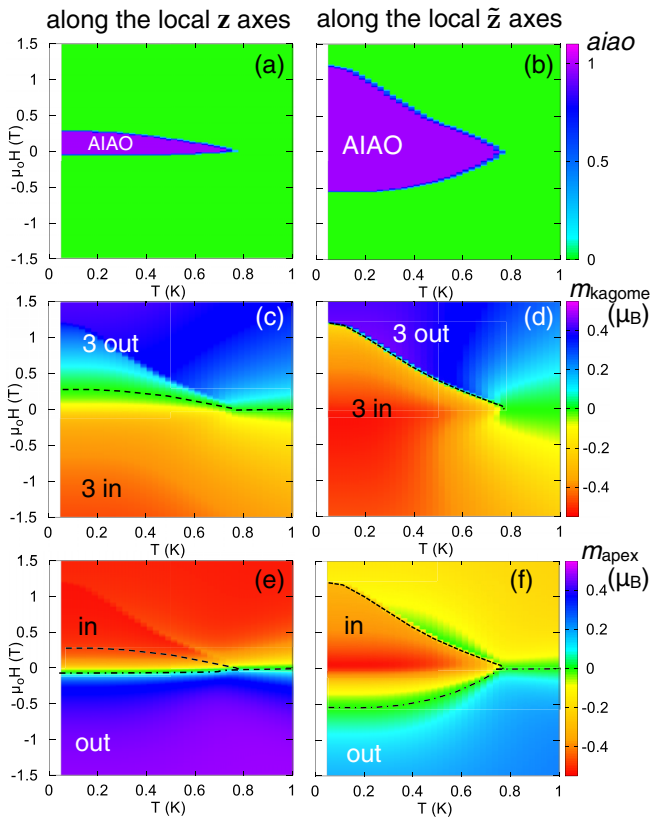

FIG. 14. Mean-field (H, T) phase diagrams obtained for $\mathbf{H} \parallel [111]$ when the field is swept from -1.5 to 1.5 T for the pure compound parameters. The left and right sides show the same results but projected along the $\mathbf{z}$ and $\tilde{\mathbf{z}}$ components of the pseudospins, respectively. (a), (b) display the *aiao* parameter; (c), (d) the kagomé spins component m_{kagome}; (e), (f) the apical spin component m_{apex}. Dashed lines are guides to the eye to show the regions delimited by the *aiao* parameter in (a) and (b).

the experiments. The right column shows the *aiao* parameter and pseudospin components along $\tilde{\mathbf{z}}$. Those are not observed in experiments but we know from calculations that they are fully AIAO ordered in zero field. In the following, a distinction will be made between the configurations with respect to $\mathbf{z}$ ($\mathbf{z}$-AIAO, for instance) and to $\tilde{\mathbf{z}}$ (denoted $\tilde{\mathbf{z}}$-AIAO).

Calculations show that the magnetic state is governed by the apical spins, as the kagomé spins simply follow the field direction [Figs. 13(c) and 13(d)]. On the contrary, the apical pseudospin is essentially along $\tilde{\mathbf{z}}$ at low field, typically below 0.5 T, hence forming tetrahedra either $\tilde{\mathbf{z}}$-all in or $\tilde{\mathbf{z}}$-all out. Above this threshold, the tetrahedra are $\tilde{\mathbf{z}}$-1I3O or $\tilde{\mathbf{z}}$-1O3I, depending on the sign of the field. Interestingly, however, even if the pseudospins are globally $\tilde{\mathbf{z}}$-AIAO, the actual magnetic configuration, i.e., with respect to $\mathbf{z}$, can be $\mathbf{z}$-1I3O (or $\mathbf{z}$-1O3I) (see Fig. 15). When comparing quantitatively with the experimental data obtained from FC measurements (see Fig. 10), the entrance in the gray region delimited by T_{m} (maximum of the susceptibility) upon cooling seems to correspond to the entrance into a $\tilde{\mathbf{z}}$-AIAO state.

Similar calculations were performed by starting from a saturated state in negative field and increasing the field, similar to the hysteresis loop/field sweeping experiments (see

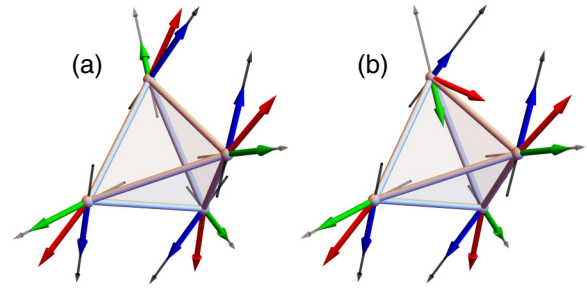

FIG. 15. Sketch of the pseudospins in a tetrahedron (a) in the blue region and (b) in the gray region of the phase diagram of Fig. 10. The black and gray arrows, respectively, represent the $\tilde{\mathbf{z}}$ and $\mathbf{z}$ local axes. Red arrows represent the total pseudospin components, the blue ones their projection on the $\tilde{\mathbf{z}}$ axes, and the green ones their projection on the $\mathbf{z}$ axes. In (a), an all out configuration is obtained for both projections, while in (b), only the $\tilde{\mathbf{z}}$ components are all out, the $\mathbf{z}$ ones being 1O3I.

Fig. 14). These calculations clearly reproduce the hysteretic behavior observed experimentally (see Fig. 7). A transition is observed at 1.2 T (right panels). It corresponds to the flipping of the kagomé spins from a $\tilde{\mathbf{z}}$-in to a $\tilde{\mathbf{z}}$-out configuration, and to a reduction of the ordered value for the apical spin. The change from the $\mathbf{z}$-AIAO to the $\mathbf{z}$-1I3O state, however, occurs gradually, the $\mathbf{z}$-AIAO component disappearing around 0.25 T (left panels). These calculations thus cannot reproduce the transition measured at about 0.1 T. To understand this discrepancy, which was not observed for the FC case, the method of the energy landscapes was used again (see Appendix D). As inferred from the experimental results and previously discussed [21], this approach reveals the presence of two local energy minima, which result in metastable states when sweeping the field. Figures 16(a) and 16(b) show the magnetic moment value associated to these local minima for the pure compound, while the color scale indicates the energy of the associated configuration. When comparing with MF calculations presented in Fig. 14, these results reveal that the magnetic moments remain trapped on a single branch, which becomes metastable for positive fields. As previously noted in Ref. [21], the jump to the lowest energy branch, i.e., the critical field obtained in the MF approach corresponds to the point ($\mu_0 H = 1.2$ T) where the metastable branch disappears. The experimental magnetic moments obtained for the pure compound from the neutron diffraction data are displayed on top of these calculated points in Figs. 16(a) and 16(b). Remarkably, the experimental points, especially for the kagomé moment, nearly fall on the calculated branches, suggesting that everything happens as if the system was jumping from the metastable branch to the minimum energy branch at a much smaller field (H_{111}), following from there the absolute energy minimum. The magnetic configuration at this jump (for the red tetrahedra) changes from a $\mathbf{z}$-all in state to a $\mathbf{z}$-1I3O configuration. The system thus reaches its equilibrium state at a much smaller field than predicted in MF and MC calculations. The associated gain in energy obtained by jumping from one branch to another at H_{111} is found to be about 50 mK, while the energy barrier between the two branches is estimated to about 1 K. This shows the existence of relaxation processes,

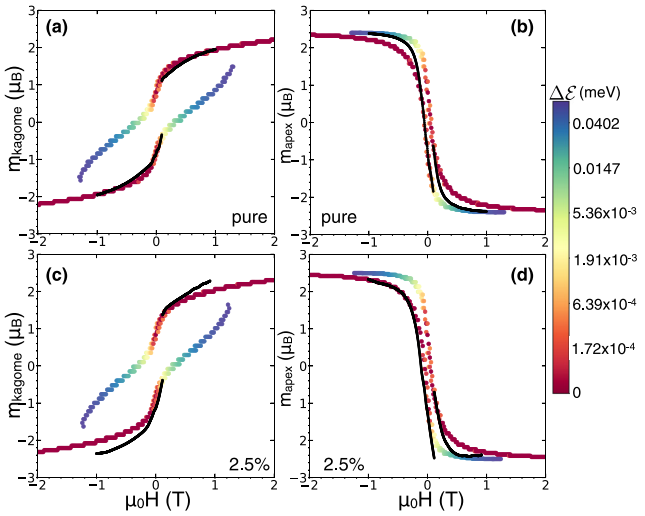

FIG. 16. Magnetic moment as a function of field for the pure [(a), (b)] and the 2.5% [(c), (d)] compounds when a field is applied along [111] for the (a)–(c) kagomé and (b)–(d) the apical spins. The color scale represents the energy difference between the calculated configuration and the absolute minimum energy configuration (logarithmic scale), the red color referring to the smallest energy. Black dots correspond to the experimental values obtained from the field-sweeping measurement analysis.

not captured by calculations, which help the system to reach its ground state. Their timescale is, however, too fast to be probed by conventional magnetization measurements. These relaxation processes may occur in regions of the sample where the barrier is weakened (close to defects or sample boundaries) or be favored by fluctuations which are not included in the calculations.

Experimentally, we have pointed out that H_1 (determined from $M(H)$ curves) and T_1 (determined from ZFC-FC curves) define the same line in the (H, T) phase diagram. Indeed, in a ZFC measurement, both $\overline{\text{AIAO}}/\overline{\text{AOAI}}$ domains are stabilized at low temperature. When applying a positive field (with our conventions) after ZFC, the all out domains of the red tetrahedra are on the equilibrium branch while the all in ones are on the metastable branch. When increasing the field and/or the temperature, the latter are suppressed. The system then reaches the equilibrium configuration when the ZFC magnetization recovers the FC equilibrium one. This occurs at the same field/temperature point in the experimental phase diagram as the magnetization jump in the hysteresis. Incidentally, at low temperature, it roughly corresponds to the point where the **z**-AIAO component disappears in the calculated FC phase diagram.

Finally, we can now understand the nature of the experimental phase diagram of Fig. 10 when the field is applied along [111] (the measurements being performed from a ZFC state or a saturated state in a negative field): in the blue region, both **z** and $\tilde{\mathbf{z}}$ components are AIAO [see the illustration in Fig. 15(a)] and the system lies in a metastable state. In the gray one, only the $\tilde{\mathbf{z}}$ component is AIAO, the **z** one being 1I3O/1O3I [see the illustration in Fig. 15(b)], and the system has reached its ground state. The microscopic mechanism at the origin of the measured values of H_1 and T_1 separating these two regions nevertheless remains an issue.

B. Role of the Ti content

In this paper, the (H, T) phase diagrams have been established for three samples, the pure $Nd_2Zr_2O_7$ compound and two Ti-substituted samples, $Nd_2(Zr_{1-x}Ti_x)_2O_7$ with $x = 2.5$ and 10%. As shown in Table II, the global pyrochlore stucture and its main properties (lattice parameter and oxygen position) are not significantly affected by the Ti substitution at low concentrations of Ti. Further structural studies are necessary to better characterize the disorder but are beyond the scope of this paper. From the present data, however, it is reasonable to consider that the titanium atoms are randomly distributed among the 16*d* sites of the crystallographic $Fd\bar{3}m$ structure.

It is worth noting that the properties of the substituted polycrystalline samples are quantitatively different from the single crystal ones (smaller θ_{CW} and slightly larger T_N and ordered moments—see Appendix B). In the literature, larger T_N and ordered moments were also reported in a pure single crystal compound [10]. The nature of the disorder and its consequences are thus not obvious but, nevertheless, two important features can be stressed: (i) The single ion properties of the neodymium ion are little affected by the presence of this disorder, the effective moment and local anisotropy being roughly similar in the three compounds. (ii) The presence of titanium is expected to mainly disturb the exchange paths, creating some distribution in the exchange parameters.

Indeed, the magnetic transition looks a bit broader in the AC susceptibility (see Fig. 3) for substituted samples but is still well defined. Strikingly, the AIAO ground state is characterized by a larger T_N along with larger critical fields than in the pure sample, suggesting that the AIAO order is more robust. Since both characteristic parameters show a maximum at 2.5% before decreasing at higher substitution concentration, the present study even suggests the existence of an optimum with respect to Ti-substitution level, where the stability of the ordered phase is best reinforced. In addition, the ordered magnetic moment is larger along the **z** direction, thus corresponding to a lower θ angle, which indicates that the disorder tends to tilt the pseudospins back toward the local $\langle 111 \rangle$ **z** axes. This picture is consistent with recent observations on Nd-based pyrochlores with a much stronger disorder on the *B* site [34–36], namely, Nd_2NbScO_7 and Nd_2GaSbO_7. In the latter, it was nevertheless pointed out that the large obtained ordered moment and transition temperature are similar to the $Nd_2Sn_2O_7$ compound [37]. It was thus proposed that the chemical pressure—which manifests in these two compounds by a small lattice parameter compared to the zirconate counterpart—is a key ingredient to understand the magnetic properties, and which could be more decisive than the disorder itself.

Despite the absence of a microscopic description of the disorder which could help solve this issue, the phase diagram of the 2.5% substituted sample can be further analyzed. To this end, we have computed the MF phase diagrams as well as the energy landscape using the exchange parameters determined by the magnetic excitations analysis [14] [see Figs. 17(a) and 17(b)]. The obtained values are $\tilde{J}_{\tilde{x}} = 0.97$, $\tilde{J}_{\tilde{y}} = 0.21$, $\tilde{J}_{\tilde{z}} =$

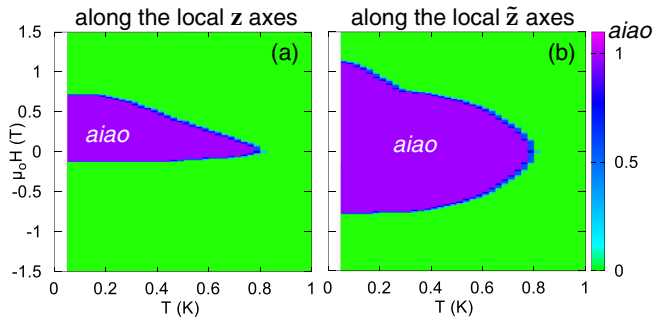

FIG. 17. (a), (b) *aiao* parameter versus (H, T) determined from mean-field calculations considering $\mathbf{H} \parallel [111]$ and swept from -1.5 to 1.5 T performed with the exchange parameters determined for the 2.5% substituted sample. (a) [respectively, (b)] shows the results for the $\mathbf{z}$ (respectively, $\tilde{\mathbf{z}}$) component of the pseudospins.

-0.53 K, $\theta = 1.08$ rad [see Eq. (1). For the sake of simplicity, $\tilde{J}_{\tilde{y}} = 0$ was assumed for energy landscape calculations.].

The first point that we stress is that, in MF calculations, the Néel temperature does not vary significantly between the results for the pure and 2.5% substituted compounds. This is not surprising since the energy range of the parameters is similar in both and the calculations strongly overestimate T_N (while MC calculations underestimate it [21]). Nevertheless, experimentally, a strong variation of T_N is observed between the three samples. This may be due to the competition at play between the Coulomb phase stabilized above the Néel temperature for the $\tilde{\mathbf{x}}$ component and the $\tilde{\mathbf{z}}$-AIAO phase [14,21] (see also Appendix A). This reminds us of the situation in $Yb_2Ti_2O_7$ [17,38–40], where the proximity of competing phases makes the transition temperature extremely sensitive to disorder. In $Nd_2Zr_2O_7$, the disorder would promote the AIAO ordering at the expense of the Coulomb phase. This manifests in the exchange parameters by a smaller ratio $\tilde{J}_{\tilde{x}}/\tilde{J}_{\tilde{z}}$ in the substituted compound, which is clearly in favor of the $\tilde{\mathbf{z}}$-AIAO phase.

When looking at the field-induced behavior, calculations qualitatively reproduce the increase of the critical fields obtained experimentally in the [001] and $[1\bar{1}0]$ directions, as well as the nature of the field-induced processes, which are similar to the pure compound. Nevertheless, there is no quantitative agreement in the obtained values for the critical field (see Table III). When the field is applied along the [111] direction, an increase of the critical field is obtained in the FC phase diagrams. Considering now the situation where the field is swept from saturation, almost no difference is obtained in the calculated critical field (of about 1.2 T) corresponding to the jump from a metastable domain to the equilibrium. When looking in more detail at the branches displayed in Figs. 16(c) and 16(d), we can see that their shape is quite different from the pure compound case, even if the two branches merge at almost the same field of about 1.2 T. The data obtained from the neutron field-sweeping analysis falls again on the branches, even if the agreement is not as good for the kagomé moment in high field. The jump from one branch to the other occurs experimentally at 0.11 T, which corresponds to an energy difference of 50 mK, comparable to the case of the pure compound.

From our experimental and calculation results, the sample comparison thus shows that despite quite strong quantitative differences in the Néel temperature or on the $\mathbf{z}$-ordered moment, the field-induced behaviors remain similar, the critical fields being shifted to larger values in the substituted samples. The level of disorder introduced in the present study on the nonmagnetic site is not strong enough to destabilize the $\tilde{\mathbf{z}}$-AIAO ordering, and on the contrary seems to reinforce it. As previously mentioned, recent studies show that the AIAO state resists to an even stronger disorder [34–36]. Consequently, it may be relevant to directly make a substitution on the magnetic site to test the stability of the AIAO state on dilution and to possibly reach the predicted quantum spin liquid ground state when the ratio $\tilde{J}_{\tilde{z}}/\tilde{J}_{\tilde{x}}$ decreases [12,41].

VI. CONCLUSION

In this paper, (H, T) phase diagrams for fields applied along the three main high-symmetry crystallographic directions have been constructed for three sample compositions of the $Nd_2(Zr_{1-x}Ti_x)_2O_7$ family. A systematic analysis of neutron diffraction data was employed, combined with low temperature magnetization measurements. Depending on the field direction, different phases are obtained, either AIAO, 2I2O, or 1I3O/1O3I. The present paper essentially establishes the stability regions of the AIAO phase and shows that a small amount of disorder further reinforces this phase, both in field and temperature. In addition, the comparison with calculations performed using the XYZ Hamiltonian shows how the field-induced phases (2I2O and 1I3O/1O3I) are connected to the two $\overline{\text{AIAO}}$ and $\overline{\text{AOAI}}$ domains and elucidates the apparent strong discrepancy between calculated and measured critical fields when the field is applied along the [111] direction. Further work on the microscopic mechanisms at play in the domain selection are nevertheless needed to quantitatively understand the critical field values.

ACKNOWLEDGMENTS

The work at the University of Warwick was supported by EPSRC, UK through Grant No. EP/T005963/1. M.L. and S.P. acknowledge financial support from the French Federation of Neutron Scattering (2FDN). M.L. acknowledges financial support from Université Grenoble-Alpes (UGA). E.L. and S.P. acknowledge financial support from ANR, France, Grant No. ANR-19-CE30-0040-02. M.L., E.L., and S.P. thank J. Debray for the orientation of the samples.

APPENDIX A: NOTES ABOUT FRAGMENTATION

Prior experimental investigations of $Nd_2Zr_2O_7$ [9,11] have pointed to the fact that the ground state of this material bears similarities with the fragmentation phenomenon exposed in Ref. [42]. In particular, the fact that only 1/3 of the total moment is ordered was one of the strongest arguments.

In this theory, the proliferation of spin flips out of the spin ice 2I2O manifold, i.e., 1O3I and 1I3O local configurations, or monopoles in the field language, produces a charged state described by two fragments that identify with the Helmholtz-Hodge decomposition of the spin ice emergent

magnetic field **M**:

$$\mathbf{M} = -\nabla\phi + \nabla \times \mathbf{A},$$

where ϕ is a scalar potential and **A** the vector potential. In this decomposition, the first term is divergence-full and carries the total gauge charge ρ, $\nabla \cdot \mathbf{M} = -\nabla \cdot \nabla\phi = \rho$. The second term $\nabla \times \mathbf{A}$ encodes the position of the spin flip and is divergenceless ($\nabla \cdot (\nabla \times \mathbf{A}) \equiv 0$). In the case of spin ice, the ground state is naturally the vacuum of charges ($\rho = 0$). However, a different ground state appears if a nonzero density of monopoles becomes favored for energetic and/or entropic reasons. Provided the fluid of monopoles crystallizes and forms a staggered pattern, the new ground state is fragmented, comprised of an AIAO component carried by the divergence full term on top of a secondary Coulomb phase carried by the divergence free term. Importantly, the charge per tetrahedron ($\rho = 2$) is only half the charge carried by a standard AIAO state ($\rho = 4$). As a result, in a neutron diffraction experiment, the fragmented state is characterized by an AIAO ordering with an ordered magnetic moment reduced by a factor of 2, on top of a spin ice pattern described by **A**.

The XYZ Hamiltonian approach is quite far away from this theory of fragmentation. Its phase diagram was studied using the gauge mean field theory (gMFT) in Refs. [18,43]. It presents unconventional $U(1)$ quantum spin-liquid states [44–50] but also includes classical states. These are ordered AIAO-like phases, with pseudo spins pointing along the $\tilde{\mathbf{x}}$, $\tilde{\mathbf{y}}$ or $\tilde{\mathbf{z}}$ direction. Considering **a** the local direction along which the pseudospins are ordered, and **b** and **c** the two other directions of the local frame, at the mean field level, these phases are stabilized provided $\tilde{J}_a < 0$ with $-1 \leqslant \frac{\tilde{J}_{b,c}}{|\tilde{J}_a|} \leqslant 3$. In Ref. [18], those states are labeled AIAO and AFO (the latter corresponding to an antiferro-octupolar state). Interestingly, the experimental couplings place $Nd_2Zr_2O_7$ close to the border between the $\tilde{x} - U(1)$ liquid phase and the $\tilde{z}$-AIAO state in the gMFT phase diagram determined by Huang *et al.* [18]. The most recent experiments actually support a picture where the paramagnetic regime above the AIAO Néel temperature in $Nd_2Zr_2O_7$ is indeed such a coulombic phase [13,14], stabilized both by the strong positive $\tilde{J}_x$ as well as entropic effects.

Reference [12] describes a MF theory of this XYZ model. For the $Nd_2Zr_2O_7$ parameters, the ground state is an AIAO magnetic configuration of the pseudospins pointing along the $\tilde{\mathbf{z}}$ axes and is thus a fully charged state. However, it turns out that the *dynamical* magnetization can still be Helmholtz-Hodge decomposed in terms of (lattice) divergence-free and divergence-full fields [12]. On the one hand, the flat spin ice mode identifies with the divergence-free *dynamical* field. Its pinch point pattern relates it to the divergence free condition $\nabla \cdot (\nabla \times \mathbf{A}) \equiv 0$. It is formed by individual precessions around the local magnetization of spins belonging to closed loops in the pyrochlore lattice. On the other hand, the dispersing branch corresponds to the divergence-full *dynamical* field and is the signature of charge propagation throughout the diamond lattice. This branch is characterized by a beautiful half-moon pattern when moving away from the pinch points. Such a pattern is typical of a curl-free condition, which characterizes the charges, since $\nabla \times (\nabla\phi) \equiv \mathbf{0}$ [51].

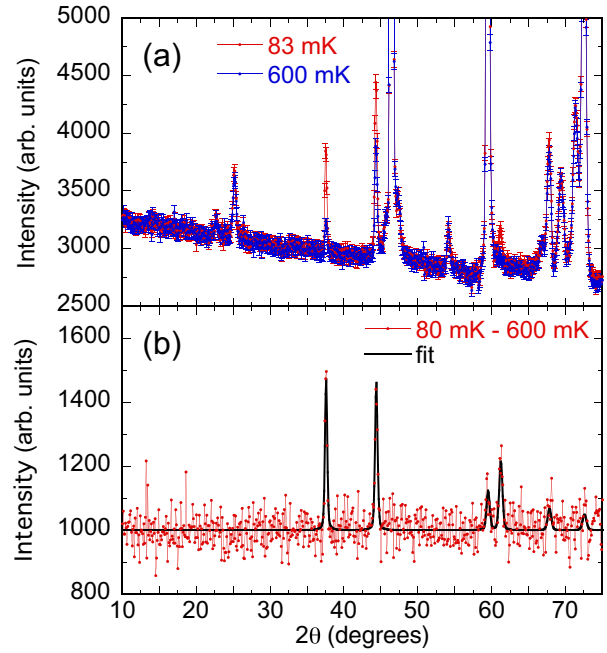

FIG. 18. (a) Powder neutron diffractograms measured on G4.1 for the $x = 2.5\%$ sample at 80 mK (red dots) and 600 mK (blue dots). (b) Difference intensity obtained when subtracting the 600 mK to the 80 mK data (red dots). The black line shows the AIAO FULLPROF refinement, giving an ordered moment of 1.36 μ_B.

APPENDIX B: POWDER SAMPLES

Aiming at a first description of the physical properties of the substituted samples, magnetic measurements along with neutron diffraction were performed on the substituted powder samples. The very low-temperature magnetization and susceptibility were measured in the same magnetometer developed at the Institut Néel as single crystals. For these measurements, the powder samples were packed in a copper pouch with apiezon grease to ensure proper thermalization. Structural parameters were obtained with the high resolution powder neutron D2B (ILL) diffractometer using $\lambda = 1.594$ Å. The ground-state magnetic structure in zero applied field was determined on the powder neutron G4.1 (LLB-Orphée, France) diffractometer using $\lambda = 2.43$ Å. A dedicated vanadium sample holder was used, loaded with ^{4}He pressure of about 10 bars to ensure thermalization. Structural and magnetic parameters were refined with the FULLPROF suite [26].

The structural data could be refined with a pyrochlore structure ($Fd\bar{3}m$ space group). Magnetic properties are qualitatively similar to the pure compound properties (see Table IV): from Curie-Weiss fits between 1.5 and 4 K, the low-temperature effective moment is estimated to 2.5 μ_B and a small (70–80 mK) but positive Curie-Weiss temperature could be extracted, indicative of effective ferromagnetic interactions. An antiferromagnetic transition is found to occur above 400 mK for both compounds in the susceptibility, but which is sharper in the 2.5%-substituted sample. Neutron diffraction refinements could show that the magnetic structure is AIAO, like in the pure compound, with an ordered moment of about $1.2 - 1.3\ \mu_B$ at low temperature (see Fig. 18).

TABLE IV. Polycrystalline parameters obtained from neutron diffraction and magnetization measurements. Structural parameters are from FULLPROF refinements at 300 K and the ordered moment is the value obtained at about 60 mK.

Powder samples	Ti concentration [%]	O(48*f*) position	Lattice parameter [Å]	T_N [mK]	θ_{CW} [mK]	μ_{eff} [μ_B]	Ordered moment [μ_B]
$Nd_2Zr_2O_7$	0	0.3366	10.69	370	225	2.42	0.8 ± 0.05
$Nd_2Zr_{1.95}Ti_{0.05}O_7$	2.8	0.3360	10.67	420	70	2.53	1.36 ± 0.04
$Nd_2Zr_{1.8}Ti_{0.2}O_7$	11.2	0.3359	10.64	430	80	2.51	1.33 ± 0.03

APPENDIX C: ANALYSIS OF THE FIELD-SWEEPING MEASUREMENTS

To complete the diffraction measurements, the intensity of selected Bragg peaks was recorded while ramping the field back and forth from −1 T to 1 T (0.015 T/min was the minimum sweeping speed) to obtain a continuous evolution versus field. The analysis of those field-sweeping measurements relies on the comparison between the experimental magnetic intensities $I^{exp}(\mathbf{Q})$ and the calculated ones $I^{calc}(\mathbf{Q})$, given the various models described in the main text and the usual definitions of the neutron intensities:

$$I^{calc}(\mathbf{Q}) = \sum_{a,b=x,y,z} \mathbf{F}^a_M(\mathbf{Q})\left(\delta_{a,b} - \frac{\mathbf{Q}^a\mathbf{Q}^b}{\mathbf{Q}^2}\right)\mathbf{F}^b_M(\mathbf{Q})^*,$$

$$\mathbf{F}_M(\mathbf{Q}) = \sum_i \mathbf{m}_i e^{i\mathbf{Q}\mathbf{R}_i}.$$

$\mathbf{m}_i$ and $\mathbf{R}_i$ denote the magnetic moment and position of the ith spin in the unit cell. The method that was developed in this paper involves the minimization of a χ^2 defined as

$$\chi^2(\mathbf{m}, H) = \sum_n (J^{calc}(\mathbf{Q}_n, \mathbf{m}) - I^{exp}(\mathbf{Q}_n, H))^2. \quad \text{(C1)}$$

$\{\mathbf{m}\}$ is the set of parameters to be refined. The n index runs over a list of $\mathbf{Q}$ vectors given in Table V and which were chosen carefully as they show a significant evolution versus field. $I^{exp}(\mathbf{Q}_n, H)$ is the experimental intensity. $J^{calc}(\mathbf{Q}_n, \mathbf{m})$ is derived from the calculated intensity $I^{calc}(\mathbf{Q})$ but is defined using the moments $\mathbf{m}_1$ and $\mathbf{m}_2$ determined with FULLPROF at two reference fields $H_1 = 0$ and $\mu_0 H_2 = \pm 1$ T:

$$J^{calc}(\mathbf{Q}_n, \mathbf{m}) = I^{exp}(\mathbf{Q}_n, H_1) + \alpha_n r_n,$$

$$r_n = I^{calc}(\mathbf{Q}_n, \mathbf{m}) - I^{calc}(\mathbf{Q}_n, \mathbf{m}_1),$$

$$\alpha_n = \frac{I^{exp}(\mathbf{Q}_n, H_2) - I^{exp}(\mathbf{Q}_n, H_1)}{I^{calc}(\mathbf{Q}_n, \mathbf{m}_2) - I^{calc}(\mathbf{Q}_n, \mathbf{m}_1)}.$$

This definition ensures that

$$J^{calc}(\mathbf{Q}_n, \mathbf{m}_1) = I^{exp}(\mathbf{Q}_n, H_1)$$

and

$$J^{calc}(\mathbf{Q}_n, \mathbf{m}_2) = I^{exp}(\mathbf{Q}_n, H_2),$$

so $\mathbf{m}_1$ and $\mathbf{m}_2$ minimize χ^2 at H_1 and H_2, respectively. This definition thus puts severe constraints on the minimization.

A homemade program was then used to calculate $\chi^2(\mathbf{m}, H)$ over a grid for the parameters $\{\mathbf{m}\}$ and to keep the values which minimize it. As different combinations of parameters can give a consistent result, a weight is associated to each solution and takes the form of a color scale in the figures presented in the main text: from blue, the worst χ^2, to red, the best χ^2. It is worth mentioning that this analysis cannot distinguish positive and negative values of the magnetic moments. A new criterion was thus added to keep only the values giving a positive product of the magnetization times the applied field (this is justified since no remanent magnetization has been observed in the magnetization curves). The points obtained with FULLPROF from the data collections at fixed fields eventually confirm the consistency of the analysis.

APPENDIX D: ENERGY LANDSCAPES

Following Ref. [21], it is instructive to calculate the energy landscape in the presence of a magnetic field to better understand the origin of the hysteresis. Writing the four spins in a tetrahedron in their local frame $(\tilde{\mathbf{x}}, \tilde{\mathbf{z}})$ as

$$\tilde{\tau} = (\sin\Phi_i, 0, \cos\Phi_i), \quad \text{(D1)}$$

the classical exchange and Zeeman energy per tetrahedron can be evaluated using the Hamiltonian given by Eqs. (1) and (2) (and neglecting the octupolar exchange $\tilde{J}_{\tilde{y}}$ term). The numerical values $\tilde{J}_{\tilde{z}} \approx -0.53$ K, $\tilde{J}_{\tilde{x}} \approx 1.18$ K, $\theta = 1.23$ rad and $\tilde{J}_{\tilde{z}} \approx -0.53$ K, $\tilde{J}_{\tilde{x}} \approx 0.97$ K, $\theta = 1.08$ rad were used,

TABLE V. List of the $\mathbf{Q}$ vectors of the magnetic Bragg peaks measured in different experiments while ramping the magnetic field.

x	**H**	**Q**
0	[001]	(2,2,0), (0,4,0), (1,1,1), (2,0,0), (3,1,−1)
	[1$\bar{1}$0]	(0,0,2), (0,0,4), (1,1,3), (2,2,0), (3,3,1), (1,1,1)
	[111]	(2,0,0), (2,−2,0), (1,−1,1), (1,3,−1)
2.5%	[001]	(2,-2,0), (0,4,0), (−1, −1, −1), (−1, 1, −1), (−3, 1, −1), (−1, −3, −1), (−3, −3, −1)
	[1$\bar{1}$0]	(0,0,2), (0,0,4), (1,1,3), (2,2,0), (3,3,1), (3,3,−1)
	[111]	(−2,0,0), (−2,2,0), (−1, 1, −1), (−1, −3,1)
10%	[001]	(2,−2,0), (0,4,0), (1,−1,1), (2,0,0), (3,1,1), (−3,3,1)
	[111]	(−2,0,0), (-2,2,0), (−1, 1, −1), (−1,-3,1)

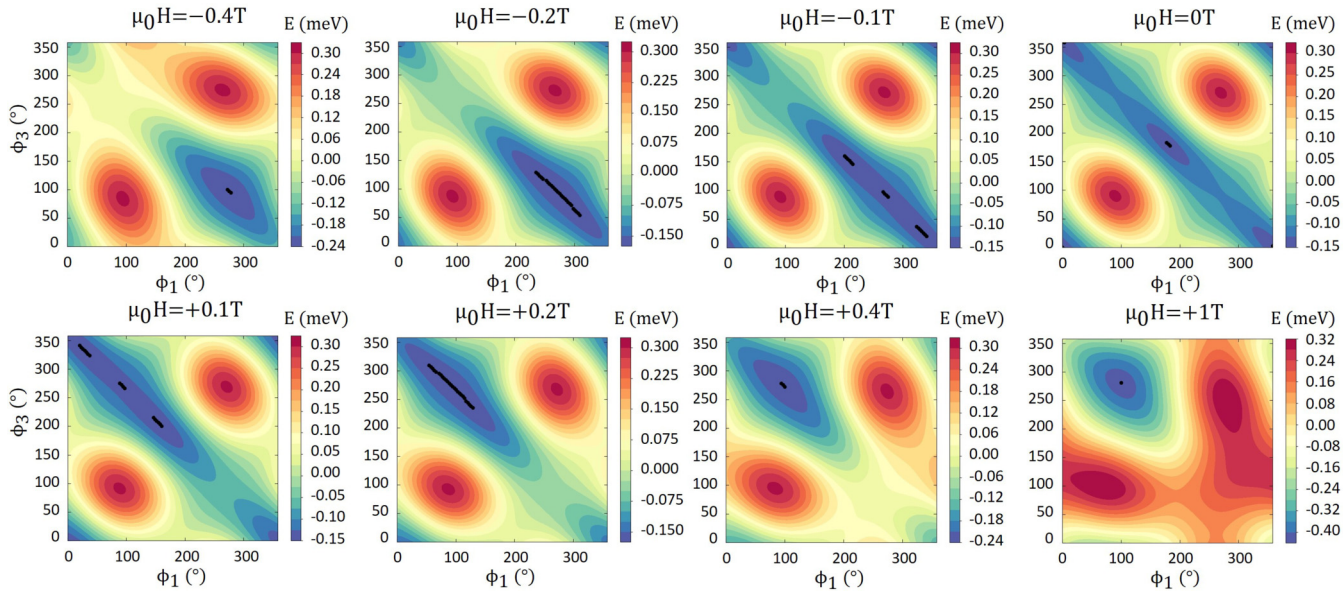

FIG. 19. Contour plot of the classical energy $\mathcal{E}$ as a function of Φ_1 and Φ_3 for $\mathbf{H} \parallel [001]$ with the pure sample exchange parameters. The black dots show the positions of the minima and the color scale displays the energy in meV.

corresponding to the pure and the 2.5% substituted sample parameters, respectively.

1. Field along [001]

In the particular case of $\mathbf{H} \parallel [001]$, the angles Φ_i are identical within the two subgroups (1,2) and (3,4), hence

$$\begin{aligned}\mathcal{E} = g_z\mu_B H\frac{2}{\sqrt{3}}(\cos(\Phi_1+\theta)-\cos(\Phi_3+\theta))\\ +2\tilde{J}_z(\cos^2\Phi_1+4\cos\Phi_1\cos\Phi_3+\cos^2\Phi_3)\\ +2\tilde{J}_x(\sin^2\Phi_1+4\sin\Phi_1\sin\Phi_3+\sin^2\Phi_3).\end{aligned}$$

At large positive field, the minimum of the energy is obtained for $\Phi_1+\theta=\pi$, $\Phi_3+\theta=0$, i.e., $\Phi_1=\pi-\theta$, $\Phi_3=-\theta$ which corresponds to the moments of the (3,4) atoms parallel to their **z** axes and the (1,2) ones antiparallel to their **z** axes. At zero field, two minima occur, corresponding to $\Phi_1=\Phi_3=0$ or π, i.e., to the domains $\overline{\text{AIAO}}$ and $\overline{\text{AOAI}}$ of the $\tilde{\mathbf{z}}$ ordered state. Figure 19 illustrates this evolution. It displays several contour plots of $\mathcal{E}$ as a function of Φ_1 and Φ_3 for the $\mathbf{H} \parallel [001]$ case. The black dots show the position of the minima. Upon increasing field, two minima appear, separate to give rise to the $\overline{\text{AIAO}}$ and $\overline{\text{AOAI}}$ domains, and finally reconnect at a higher field. With a sufficiently large field, a single solution survives.

2. Field along [111]

For $\mathbf{H} \parallel [111]$, the angles Φ_i are identical for the kagomé spins and we are left with two variables Φ_1 (kagomé) and Φ_2 (apical). The classical energy writes

$$\begin{aligned}\mathcal{E} = g_z\mu_B H[-\cos(\Phi_1+\theta)+\cos(\Phi_2+\theta)]\\ +6\tilde{J}_z(\cos^2\Phi_1+\cos\Phi_1\cos\Phi_2)\\ +6\tilde{J}_x(\sin^2\Phi_1+\sin\Phi_1\sin\Phi_2).\end{aligned}$$

At large positive field, the minimum of the energy is obtained for $\Phi_1+\theta=0$, $\Phi_2+\theta=\pi$, i.e., $\Phi_1=-\theta$, $\Phi_2=\pi-\theta$, which corresponds to spins 1, 3, 4 parallel to their **z** axes and spin 2 antiparallel to its **z** axis. At zero field, two minima occur, corresponding to $\Phi_1=\Phi_3=0$ or π, i.e., to the two domains of the AIAO configuration.

3. Field along [1$\bar{1}$0]

For $\mathbf{H} \parallel [1\bar{1}0]$, two different regimes can be considered. At large fields, $|H| \geqslant H_{110}$, $\Phi_2=\pi+\Phi_1$ and $\Phi_3=\pi+\Phi_4$, hence the classical energy

$$\begin{aligned}\mathcal{E} = g_z\mu_B H 2\sqrt{\frac{2}{3}}\cos(\Phi_3+\theta)\\ -2\tilde{J}_z(\cos^2\Phi_1+\cos^2\Phi_3)\\ -2\tilde{J}_x(\sin^2\Phi_1+\sin^3\Phi_3).\end{aligned}$$

At large positive field, the minimum of the energy is obtained for $\Phi_3+\theta=\pi$, i.e., $\Phi_3=\pi-\theta$, $\Phi_4=-\theta$ which corresponds to spin 3 antiparallel to its **z** axis and spin 4 parallel to its **z** axis.

At small fields, $|H| \leqslant H_{110}$, no simplification appears but $\Phi_1=\Phi_2$ and we are left with three independent variables $\Phi_{1,3,4}$. The classical energy writes

$$\begin{aligned}\mathcal{E} = g_z\mu_B H\sqrt{\frac{2}{3}}(\cos(\Phi_3+\theta)-\cos(\Phi_4+\theta))\\ +2\tilde{J}_z(\cos^2\Phi_1+2\cos\Phi_1(\cos\Phi_3+\cos\Phi_4)\\ +\cos\Phi_3\cos\Phi_4)\\ +2\tilde{J}_x(\sin^2\Phi_1+2\sin\Phi_1(\sin\Phi_3+\sin\Phi_4)\\ +\sin\Phi_3\sin\Phi_4).\end{aligned}$$

The minimization of $\mathcal{E}$ in the general case should be carried out in the three-dimensional space spanned by the three Φ_i angles.

[1] *Introduction to Frustrated Magnetism*, edited by C. Lacroix, P. Mendels, and F. Mila (Springer-Verlag, Berlin, 2011).

[2] M. J. P. Gingras and P. A. McClarty, Quantum spin ice: A search for gapless quantum spin liquids in pyrochlore magnets, Rep. Prog. Phys. **77**, 056501 (2014).

[3] J. S. Gardner, M. J. P. Gingras, and J. E. Greedan, Magnetic pyrochlore oxides, Rev. Mod. Phys. **82**, 53 (2010).

[4] M. J. Harris, S. T. Bramwell, D. F. McMorrow, T. Zeiske, and K. W. Godfrey, Geometrical Frustration in the Ferromagnetic Pyrochlore $Ho_2Ti_2O_7$, Phys. Rev. Lett. **79**, 2554 (1997).

[5] A. P. Ramirez, A. Hayashi, R. J. Cava, R. Siddharthan, and B. S. Shastry, Zero-point entropy in 'spin ice', Nature **399**, 333 (1999).

[6] C. L. Henley, Power-law spin correlations in pyrochlore antiferromagnets, Phys. Rev. B **71**, 014424 (2005).

[7] S. V. Isakov, K. Gregor, R. Moessner, and S. L. Sondhi, Dipolar Spin Correlations in Classical Pyrochlore Magnets, Phys. Rev. Lett. **93**, 167204 (2004).

[8] T. Fennell, P. P. Deen, A. R. Wildes, K. Schmalzl, D. Prabhakaran, A. T. Boothroyd, R. J. Aldus, D. F. McMorrow, and S. T. Bramwell, Magnetic Coulomb phase in the spin ice $Ho_2Ti_2O_7$, Science **326**, 415 (2009).

[9] E. Lhotel, S. Petit, S. Guitteny, O. Florea, M. Ciomaga Hatnean, C. Colin, E. Ressouche, M. R. Lees, and G. Balakrishnan, Fluctuations and All-In–All-Out Ordering in Dipole-Octupole $Nd_2Zr_2O_7$, Phys. Rev. Lett. **115**, 197202 (2015).

[10] J. Xu, V. K. Anand, A. K. Bera, M. Frontzek, D. L. Abernathy, N. Casati, K. Siemensmeyer, and B. Lake, Magnetic structure and crystal field states of the pyrochlore antiferromagnet $Nd_2Zr_2O_7$, Phys. Rev. B **92**, 224430 (2015).

[11] S. Petit, E. Lhotel, B. Canals, M. Ciomaga Hatnean, J. Ollivier, H. Mutka, E. Ressouche, A. R. Wildes, M. R. Lees, and G. Balakrishnan, Observation of magnetic fragmentation in spin ice, Nat. Phys. **12**, 746 (2016).

[12] O. Benton, Quantum origins of moment fragmentation in $Nd_2Zr_2O_7$, Phys. Rev. B **94**, 104430 (2016).

[13] J. Xu, O. Benton, A. T. M. N. Islam, T. Guidi, G. Ehlers, and B. Lake, Order Out of a Coulomb Phase and Higgs Transition: Frustrated Transverse Interactions of $Nd_2Zr_2O_7$, Phys. Rev. Lett. **124**, 097203 (2020).

[14] M. Léger, E. Lhotel, M. Ciomaga Hatnean, J. Ollivier, A. R. Wildes, S. Raymond, E. Ressouche, G. Balakrishnan, and S. Petit, Spin Dynamics and Unconventional Coulomb Phase in $Nd_2Zr_2O_7$, Phys. Rev. Lett. **126**, 247201 (2021).

[15] T. Taniguchi, H. Kadowaki, H. Takatsu, B. Fåk, J. Ollivier, T. Yamazaki, T. J. Sato, H. Yoshizawa, Y. Shimura, T. Sakakibara, T. Hong, K. Goto, L. R. Yaraskavitch, and J. B. Kycia, Long-range order and spin-liquid states of polycrystalline $Tb_{2+x}Ti_{2-x}O_{7+y}$, Phys. Rev. B **87**, 060408(R) (2013).

[16] M. Shirai, R. S. Freitas, J. Lago, S. T. Bramwell, C. Ritter, and I. Živković, Doping-induced quantum crossover in $Er_2Ti_{2-x}Sn_xO_7$, Phys. Rev. B **96**, 180411(R) (2017).

[17] K. E. Arpino, B. A. Trump, A. O. Scheie, T. M. McQueen, and S. M. Koohpayeh, Impact of stoichiometry of $Yb_2Ti_2O_7$ on its physical properties, Phys. Rev. B **95**, 094407 (2017).

[18] Y.-P. Huang, G. Chen, and M. Hermele, Quantum Spin Ices and Topological Phases from Dipolar-Octupolar Doublets on the Pyrochlore Lattice, Phys. Rev. Lett. **112**, 167203 (2014).

[19] L. Opherden, J. Hornung, T. Herrmannsdörfer, J. Xu, A. T. M. N. Islam, B. Lake, and J. Wosnitza, Evolution of antiferromagnetic domains in the all-in-all-out ordered pyrochlore $Nd_2Zr_2O_7$, Phys. Rev. B **95**, 184418 (2017).

[20] A weak contribution to the neutron scattering cross section is expected at large wave vectors.

[21] J. Xu, O. Benton, V. K. Anand, A. T. M. N. Islam, T. Guidi, G. Ehlers, E. Feng, Y. Su, A. Sakai, P. Gegenwart, and B. Lake, Anisotropic exchange Hamiltonian, magnetic phase diagram, and domain inversion of $Nd_2Zr_2O_7$, Phys. Rev. B **99**, 144420 (2019).

[22] M. Ciomaga Hatnean, M. R. Lees, and G. Balakrishnan, Growth of single-crystals of rare-earth zirconate pyrochlores, $Ln_2Zr_2O_7$ (with Ln = La, Nd, Sm, and Gd) by the floating zone technique, J. Cryst. Growth **418**, 1 (2015).

[23] M. Ciomaga Hatnean, C. Decorse, M. R. Lees, O. A. Petrenko, and G. Balakrishnan, Zirconate pyrochlore frustrated magnets: Crystal growth by the floating zone technique, Crystals **6**, 79 (2016).

[24] C. Paulsen, DC magnetic measurments, in *Introduction to Physical Techniques in Molecular Magnetism: Structural and Macroscopic Techniques* (Publication Service of the University of Zaragoza, Zaragoza, 2001), p. 1.

[25] A. Aharoni, Demagnetizing factors for rectangular ferromagnetic prisms, J. App. Phys. **83**, 3432 (1998).

[26] J. Rodriguez-Carvajal, Recent advances in magnetic structure determination by neutron powder diffraction, Physica B **192**, 55 (1993).

[27] M. J. Harris, S. T. Bramwell, P. C. W. Holdsworth, and J. D. M. Champion, Liquid-Gas Critical Behavior in a Frustrated Pyrochlore Ferromagnet, Phys. Rev. Lett. **81**, 4496 (1998).

[28] It is worth mentioning that in a trial experiment where the field was not perfectly aligned along $[1\bar{1}0]$ (about 4 degrees while less than 1 in the present experiment), such a nonzero moment could be refined, suggesting that it is likely a byproduct of the ill-aligned component of the field.

[29] J. Xu, A. T. M. N. Islam, I. N. Glavatskyy, M. Reehuis, J. U. Hoffmann, and B. Lake, Field induced quantum spin 1/2 chains and disorder in $Nd_2Zr_2O_7$, Phys. Rev. B **98**, 060408(R) (2018).

[30] E. Lhotel, S. Petit, M. Ciomaga Hatnean, J. Ollivier, H. Mutka, E. Ressouche, M. R. Lees, and G. Balakrishnan, Evidence for dynamic kagome ice, Nat. Commun. **9**, 3786 (2018).

[31] L. Opherden, T. Bilitewski, J. Hornung, T. Herrmannsdörfer, A. Samartzis, A. T. M. N. Islam, V. K. Anand, B. Lake, R. Moessner, and J. Wosnitza, Inverted hysteresis and negative remanence in a homogeneous antiferromagnet, Phys. Rev. B **98**, 180403(R) (2018).

[32] P. C. Guruciaga, M. Tarzia, M. V. Ferreyra, L. F. Cugliandolo, S. A. Grigera, and R. A. Borzi, Field-Tuned Order by Disorder in Frustrated Ising Magnets with Antiferromagnetic Interactions, Phys. Rev. Lett. **117**, 167203 (2016).

[33] B. Placke, R. Moessner, and O. Benton, Hierarchy of energy scales and field-tunable order by disorder in dipolar-octupolar pyrochlores, Phys. Rev. B **102**, 245102 (2020).

[34] C. Mauws, N. Hiebert, M. Rutherford, H. D. Zhou, Q. Huang, M. B. Stone, N. P. Butch, Y. Su, E. S. Choi, Z. Yamani, and C. R. Wiebe, Magnetic ordering in the Ising antiferromagnetic pyrochlore Nd_2ScNbO_7, J. Phys.: Condens. Matter **33**, 245802 (2021).

[35] A. Scheie, M. Sanders, Y. Qiu, T. Prisk, R. Cava, and C. Broholm, Beyond magnons in Nd_2ScNbO_7: An Ising

pyrochlore antiferromagnet with all in all out order and random fields, arXiv:2102.13656.

[36] S. J. Gomez, P. M. Sarte, M. Zelensky, A. M. Hallas, B. A. Gonzalez, K. H. Hong, E. J. Pace, S. Calder, M. B. Stone, Y. Su, E. Feng, M. D. Le, C. Stock, J. P. Attfield, S. D. Wilson, C. R. Wiebe, and A. A. Aczel, Absence of moment fragmentation in the mixed *B*-site pyrochlore Nd_2GaSbO_7, Phys. Rev. B **103**, 214419 (2021).

[37] A. Bertin, P. Dalmas de Réotier, B. Fåk, C. Marin, A. Yaouanc, A. Forget, D. Sheptyakov, B. Frick, C. Ritter, A. Amato, C. Baines, and P. J. C. King, $Nd_2Sn_2O_7$: An all-in—all-out pyrochlore magnet with no divergence-free field and anomalously slow paramagnetic spin dynamics, Phys. Rev. B **92**, 144423 (2015).

[38] J. Robert, E. Lhotel, G. Remenyi, S. Sahling, I. Mirebeau, C. Decorse, B. Canals, and S. Petit, Spin dynamics in the presence of competing ferromagnetic and antiferromagnetic correlations in $Yb_2Ti_2O_7$, Phys. Rev. B **92**, 064425 (2015).

[39] L. D. C. Jaubert, O. Benton, J. G. Rau, J. Oitmaa, R. R. P. Singh, N. Shannon, and M. J. P. Gingras, Are Multiphase Competition and Order by Disorder the Keys to Understanding $Yb_2Ti_2O_7$? Phys. Rev. Lett. **115**, 267208 (2015).

[40] A. Scheie, J. Kindervater, S. Zhang, H. J. Changlani, G. Sala, G. Ehlers, A. Heinemann, G. S. Tucker, S. M. Koohpayeh, and C. Broholm, Multiphase magnetism in $Yb_2Ti_2O_7$, Proc. Natl. Acad. Sci. USA **117**, 27245 (2020).

[41] O. Benton, Ground-state phase diagram of dipolar-octupolar pyrochlores, Phys. Rev. B **102**, 104408 (2020).

[42] M. E. Brooks-Bartlett, S. T. Banks, L. D. C. Jaubert, A. Harman-Clarke, and P. C. W. Holdsworth, Magnetic Moment Fragmentation and Monopole Crystallization, Phys. Rev. X **4**, 011007 (2014).

[43] Y.-D. Li and G. Chen, Symmetry enriched $U(1)$ topological orders for dipole-octupole doublets on a pyrochlore lattice, Phys. Rev. B **95**, 041106(R) (2017).

[44] M. Hermele, M. P. A. Fisher, and L. Balents, Pyrochlore photons: The $U(1)$ spin liquid in a $S = 1/2$ three-dimensional frustrated magnet, Phys. Rev. B **69**, 064404 (2004).

[45] N. Shannon, O. Sikora, F. Pollmann, K. Penc, and P. Fulde, Quantum Ice: A Quantum Monte Carlo Study, Phys. Rev. Lett. **108**, 067204 (2012).

[46] O. Benton, O. Sikora, and N. Shannon, Seeing the light: Experimental signatures of emergent electromagnetism in a quantum spin ice, Phys. Rev. B **86**, 075154 (2012).

[47] L. Savary and L. Balents, Coulombic Quantum Liquids in Spin-1/2 Pyrochlores, Phys. Rev. Lett. **108**, 037202 (2012).

[48] L. Savary and L. Balents, Spin liquid regimes at nonzero temperature in quantum spin ice, Phys. Rev. B **87**, 205130 (2013).

[49] Z. Hao, A. G. R. Day, and M. J. P. Gingras, Bosonic many-body theory of quantum spin ice, Phys. Rev. B **90**, 214430 (2014).

[50] C.-J. Huang, Y. Deng, Y. Wan, and Z. Y. Meng, Dynamics of Topological Excitations in a Model Quantum Spin Ice, Phys. Rev. Lett. **120**, 167202 (2018).

[51] H. Yan, R. Pohle, and N. Shannon, Half moons are pinch points with dispersion, Phys. Rev. B **98**, 140402(R) (2018).